

Universidade de Lisboa
Faculdade de Ciências
Departamento de Física



Partial volume correction using bimodal contrast agents in PET-MRI

Carla Alexandra Gonçalves Semedo

DISSERTAÇÃO

MESTRADO INTEGRADO EM ENGENHARIA BIOMÉDICA E
BIOFÍSICA

PERFIL EM SINAIS E IMAGENS MÉDICAS

2014

Universidade de Lisboa
Faculdade de Ciências
Departamento de Física



Partial volume correction using bimodal contrast agents in PET-MRI

Carla Alexandra Gonçalves Semedo

DISSERTAÇÃO

MESTRADO INTEGRADO EM ENGENHARIA BIOMÉDICA E
BIOFÍSICA

PERFIL EM SINAIS E IMAGENS MÉDICAS

Orientador Externo: Professor Doutor Rafael Torres Martin de Rosales
Orientador Interno: Professor Doutor Alexandre Andrade

2014

Acknowledgements

This project was done in collaboration with several people at King's College London - Division of Imaging Sciences & Biomedical Engineering and Faculty of Sciences, University of Lisbon.

First of all, I would like to thank to my external supervisor Dr Rafael Rosales for letting me doing a research project in PET-MR and nanoparticles areas, as well as for showing me how important and fascinating multimodal imaging agents are.

Secondly, I would like to express my special thanks to Dr Istvan Szanda for guiding me through the Biomedical aspects of the work developed and showed me how interesting and relevant Partial Volume Correction is. I really appreciate the knowledge shared and all the comments made.

This project also would not have been possible without the contribution of Dr Charalampos Tsoumpas who helped me during the initial stage of this project and introduced me the PVC field.

I would also like to thank Dr Miho Shidahara for helping me with the Partial Volume Correction method used in this project and with the results obtained. I am very grateful for all the explanations given.

Additionally, I would like to express my gratitude towards my internal supervisor, Professor Alexandre Andrade. Two years ago, he gave me the opportunity to develop a project about MRI and schizophrenia. It was really important for defining my future aspirations which are doing research in MRI and neurology areas. Also, I would like to thank him for all the support and feedback given throughout my course and thesis.

I do consider that this Master project was an unique experience. I was able to put my interest in MRI and nanoparticles into practice, learn about image processing, and get in touch with PET and Partial Volume Correction (PVC).

All these aspects resulted in an improvement of my knowledge and interest in continuing working with bimodal nanoparticles (both detectable by PET and MRI) and PVC procedures.

Finally, I am very grateful to my family and friends for being always by my side and for making the difference in the good and bad moments of my life.

Resumo

Tomografia por Emissão de Positrões (PET, do Inglês *Positron Emission Tomography*) é uma técnica de medicina nuclear que se baseia no uso de radiofármacos, permitindo o estudo de mecanismos metabólicos. Os radionuclídeos emitem positrões no decorrer do tempo, os quais definem uma determinada trajectória até se aniquilarem com os electrões presentes no meio, originando dois fotões γ com 511 keV de energia que serão detectados pelo sistema de PET. Assim, é possível a obtenção de imagens funcionais para fins de diagnóstico de diversas patologias.

Todavia, as imagens de PET são caracterizadas por uma baixa resolução espacial em virtude de vários factores:

- Alcance dos positrões;
- Efeito de Compton que corresponde à deflexão na trajectória dos fotões γ ;
- Atenuação dos fotões gama;
- Movimento do paciente, batimento cardíaco e respiração.

Todos estes factores são responsáveis pela ocorrência de PVEs (do Inglês, *Partial Volume Effects*) que corresponde à perda de detalhe e/ou aparente actividade em pequenos objectos ou regiões nas imagens médicas. De forma a minimizar o impacto de PVEs na qualidade das imagens de PET, vários procedimentos designados de PVC (do Inglês, *Partial Volume Correction*) têm sido desenvolvidos.

Por outro lado, cada técnica de imagiologia permite a obtenção de imagens funcionais e/ou anatómicas para aplicações bem específicas, contudo todas elas apresentam limitações. Neste contexto, imagiologia por intermédio de agentes bi- ou multimodais surgiu como meio de estudo dos processos biológicos para fins de investigação, diagnóstico e terapia, uma vez que as potencialidades de várias técnicas de imagiologia são exploradas em um único agente, garantindo a obtenção de dados mais precisos.

Tendo em conta a baixa resolução das imagens de PET e as vantagens dos agentes bimodais, este projecto teve como objectivo avaliar a associação de nanopartículas detectáveis por PET e Ressonância Magnética (MRI, do Inglês *Magnetic Resonance Imaging*) e procedimentos de PVC para melhorar a qualidade das imagens de PET. Mais especificamente, como base deste projecto foram utilizadas nanopartículas SPIO (Superparamagnetic Iron Oxide) associadas a Flúor-18 (^{18}F) e o método de PVC denominado SFSRR (Structural and Functional Information for Resolution Recovery).

SFSRR foi seleccionado como método de PVC a utilizar neste projecto, uma vez que este procedimento já demonstrou resultados promissores em estudos neurológicos de PET quando comparado com outras metodologias *standard* de PVC, nomeadamente as técnicas de deconvolução van Cittert e Lucy-Richardson e o procedimento GTM (Geometrix Transfer Matrix). [32, 67, 68].

A realização deste projecto envolveu quatro fases: (i) realização de uma simulação para entendimento do funcionamento do método de SFSRR; (ii) aquisição de imagens de PET e MRI de um fantoma utilizando um scanner nanoPET/MRI; (iii) definição de um protocolo para processamento dos dados de fantoma e (iv) aplicação do procedimento SFSRR a dados simulados e de fantoma.

O Capítulo 2 inicia-se com a apresentação dos princípios básicos de PET, dando especial ênfase aos factores que afectam a qualidade das imagens desta técnica (Secção 2.1.3). Por sua vez, são abordados os conceitos relacionados com sistemas PET/MRI, agentes de contraste detectáveis por PET e MRI e por fim PVC.

No Capítulo 3 é descrito o trabalho desenvolvido no decorrer deste projecto, mais especificamente a simulação realizada, estratégias seguidas para processamento dos dados de fantoma e por fim a aplicação do método SFSRR a dados simulados e de fantoma.

A simulação realizada consistiu em um quadrado cujos voxéis possuíam a mesma intensidade 1000 e no exterior 0. Para recriar a baixa resolução espacial de PET um filtro Gaussiano foi aplicado, resultando num dos ficheiros de entrada do método SFSRR denominado *PET data*. Os outros dois ficheiros de entrada foram obtidos: (i) ao estimar-se a média dos vóxeis situados no interior do quadrado em *PET data*, originando *Segmented PET data* e (ii) aplicação de um filtro Gaussiano a *Segmented PET data* resultando no último ficheiro de entrada designado *Smoothed Segmented PET data*. Estes três ficheiros foram considerados para efectuar a melhoria de qualidade de *PET data*.

Em termos dos dados reais, os três principais objectivos estudados foram:

- Verificar como o tamanho do objecto influencia a PVC efectuada;
- Analisar a eficiência do procedimento de SFSRR quando várias concentrações de nanopartículas e ^{18}F são utilizadas;
- Examinar como a filtragem afecta os resultados obtidos com o método SFSRR.

Assim, um *Cucumis sativus* (pepino) foi utilizado como fantoma no qual no seu interior continha doze tubos com três possíveis diâmetros, com o intuito de explorar a relação entre a dimensão do objecto e PVC:

- Tubo pequeno - 0.5 mm de diâmetro;
- Tubo médio - 1 mm de diâmetro;
- Tubo grande - 1.5 mm de diâmetro.

Todos os tubos possuíam soluções de nanopartículas associadas a Fluór-18, com excepção de dois que continham água, solução a considerar como referência.

Tal visou estudar como é que a concentração de radioisótopo e nanopartículas influencia os resultados de PVC.

O último aspecto analisado foi como a filtragem está relacionada com a melhoria da qualidade das imagens de PET. Para tal, valores distintos de filtragem foram utilizados num dos ficheiros de entrada do procedimento de SFSRR, mais especificamente *Smoothed Segmented PET*.

Os dados reais foram adquiridos ao realizar-se um exame simultâneo de PET-MRI durante 63 minutos em um scanner Mediso nanoPET/MRI. Imagens ponderadas em T_2 foram obtidas de forma a explorar a capacidade de contraste por T_2 das nanopartículas SPIO, possibilitando determinar a exacta localização espacial dos doze tubos. Por outro lado, as imagens de PET permitiram inferir a actividade de ^{18}F existente em cada um dos tubos.

O método de SFSRR foi desenvolvido de forma a ser aplicado em imagens neurológicas de PET, sendo que o procedimento inclui uma estratégia para processamento dos dados de PET e MRI antes de efectuar-se a melhoria das imagens de PET. Todavia, uma vez que neste projecto foram utilizados dados de fantoma, uma das etapas do trabalho desenvolvido consistiu na definição de um protocolo de processamento dos dados.

O protocolo de processamento definido incluiu três *softwares*: (i) VivoQuant; (ii) Fiji e (iii) MATLAB.

VivoQuant automaticamente altera as dimensões e tamanho dos vóxeis dos dados de PET, de forma a coincidir com as características da imagem de referência, neste caso MRI. Igualmente, é possível reorientar os dados e realizar transformações espaciais com os dois tipos de dados presentes na mesma janela, minimizando a ocorrência de erros no decorrer desta etapa.

Por outro lado, Fiji foi utilizado para desenhar áreas de interesse uma vez que este *software* possui uma grande variedade de formas e ferramentas para este efeito. Outra vantagem é a existência do *plugin* denominado MIJ que permite a leitura e troca de dados entre Fiji e MATLAB.

Seguidamente, MATLAB foi seleccionado para: (i) aplicar uma máscara aos dados de PET com o intuito de seleccionar-se somente as contagens de PET situadas no interior dos tubos; (ii) estimação da média em cada tubo; (iii) filtragem dos dados e (iv) exportar dados no formato Analyze e tipo *double*.

Assim, os três ficheiros de entrada do método SFSRR foram criados - *PET*, *Segmented PET* and *Smoothed Segmented PET* - e foi possível efectuar PVC do ficheiro *PET*.

Os resultados obtidos e respectiva discussão são mencionados no Capítulo 4.

A simulação realizada demonstrou que o procedimento de SFSRR levou a uma melhoria nos valores máximo e média de PET, em aproximadamente 6.8% e 10.3%. Igualmente, os dados simulados foram criados de tal forma que todas as fatias tivessem a mesma distribuição de intensidades, contudo a imagem obtida após a aplicação do método de SFSRR não apresenta esta uniformidade o qual não era esperado. O esclarecimento desta questão será alvo de estudo futuro.

Seguidamente, o trabalho desenvolvido focou-se na análise de dados de fantoma. A existência de PVEs é mais significativa para objectos de pequenas dimensões e na presença de maiores valores de filtragem. Os resultados obtidos com o fantoma revelaram maiores diferenças nas contagens de PET em tubos de menores dimensões contendo maiores concentrações de nanopartículas e ^{18}F , assim como quando maiores valores de filtragem foram considerados. Além disso, nos outros dois tipos de tubos - médio e grande - as maiores melhorias nas

contagens foram observadas para menores concentrações de SPIOs e ^{18}F , bem como para valores superiores de filtragem.

Por fim, conclusões e perspectivas futuras são apresentadas no Capítulo 5.

Os resultados obtidos demonstraram que o procedimento de SFSRR é eficiente para minimizar a influência de PVEs nas imagens de PET. Todavia, é importante realçar que o procedimento SFSRR foi desenvolvido de forma a ser utilizado em estudos neurológicos de PET, pelo que os parâmetros existentes estão optimizados para esta aplicação. Assim, futuramente vários parâmetros terão de ser alterados com vista a que o método seja adaptado aos dados de fantoma utilizados no decorrer deste projecto. Igualmente, mais estudos com dados simulados e reais terão de ser efectuados para melhor entender-se os resultados iniciais.

Palavras-chave: Nanopartículas bimodais; Tomografia por Emissão de Positrões; PVC; SFSRR.

Abstract

Positron emission tomography (PET) images are characterized by a low spatial resolution mainly due to: (i) radioisotopes' positron ranges; (ii) scatter; (iii) attenuation; (iv) parallax error or radial elongation and (v) motion. Due to these aspects, partial volume effects (PVEs) can occur which are characterized by loss of detail and/or apparent activity in small objects or regions at spatial and/or time levels. Partial Volume Correction (PVC) methodologies aim to minimize the impact of PVEs in PET images [4, 8, 73].

Also, dual- or multi-modality imaging arise from the combination of two or more imaging techniques based on the use of multi-modal probes, ensuring a better visualization of biological processes and acquisition of more accurate data.

In this context, this project aimed to evaluate the potential of combining PET/MRI nanoprobe and PVC procedures for improving the quality of PET images. More specifically, superparamagnetic iron oxide (SPIO) nanoparticles combined to ^{18}F radioisotope and the PVC method named SFSRR (Structural and Functional Information for Resolution Recovery) were used as basis of the work developed in this project [32, 67, 68].

The simulation study performed showed that the SFSRR procedure led to an average improvement of 6.8% in maximum and 10.3% in mean values. Additionally, the tracer's activity distribution was equivalent in all slices of each input data, however this uniformity was not observed in recovered data. Thus, this aspect will be clarified in future work.

PVEs are more significant for smaller objects and greater smoothing values. Phantom data results demonstrated larger uptake differences in small tubes containing a higher concentration of SPIO- ^{18}F and for greater smoothing values. In contrast, higher quantification deviations in medium and big tubes were detected for lower isotopes' concentrations and greater smoothing values, especially in medium tubes.

The results obtained showed that the SFSRR procedure is efficient for minimizing the influence of PVEs in PET images. Nevertheless, further experiments are required for better understanding the initial results.

Keywords: bimodal nanoparticle imaging agents; PET; Partial Volume Correction; SFSRR.

Contents

Acknowledgements	i
Resumo	iii
Abstract	viii
Acronyms	xii
List of Figures	xv
List of Tables	xvii
1 Introduction	1
2 Theoretical Background	3
2.1 Positron Emission Tomography	3
2.1.1 Radionuclides and Positron Emission Decay	3
2.1.2 Detection of gamma photons	5
2.1.3 Image Quality	8
2.2 PET/MRI Systems	10
2.3 Contrast Agents	13
2.3.1 Nanoparticles	13
2.3.2 MRI contrast agents	14
2.3.3 PET/MRI nanoparticle agents	15
2.4 Partial Volume Correction (PVC)	16
2.4.1 Partial Volume Effects	16
2.4.2 PVC procedures	18
2.4.3 Efficiency of PVC procedures	21
2.4.4 Applications of PVC	22
2.4.5 Structural and Functional Information for Resolution Recovery (SFSRR)	22
2.5 PET/MRI nanoprobe studies	24
2.5.1 PET/MRI nanoprobe	24
2.5.2 PET/MRI nanoprobe and PVC	25
3 Materials and Methods	26
3.1 SFSRR procedure - original processing protocol	26
3.2 Simulated Data	28
3.2.1 Data creation	28

3.2.2	Partial Volume Correction using SFSRR procedure	30
3.3	Phantom Data	31
3.3.1	Mediso nanoScan PET/MRI scanner	31
3.3.2	Data	32
3.3.3	Experiments for defining an Image Processing protocol . .	33
3.3.4	Final Image Processing protocol	38
3.3.5	Partial Volume Correction using SFSRR procedure	44
4	Results and Discussion	45
4.1	Simulated data	45
4.1.1	Intensity Range	45
4.1.2	Intensity differences in the different slices	47
4.1.3	Partial Volume Correction	49
4.2	Phantom data	50
4.2.1	Intensity Range	50
4.2.2	Partial Volume Correction	52
5	Conclusion	62
A	Simulated data - Results	64
B	Phantom data - Results	65
	Bibliography	69

Acronyms

2D	Two-Dimensional
3D	Three-Dimensional
adjMC	Adjoint Monte Carlo
CT	Computed Tomography
DICOM	Digital Imaging and Communications in Medicine
FWHM	Full-Width-Half-Maximum
GTM	Geometric Transfer Matrix
LOR	Line-Of-Response
MAP	Maximum a Posteriori
ML-EM	Maximum Likelihood Estimation Method
MR	Magnetic Resonance
MRA	Multiresolution Analysis
MRI	Magnetic Resonance Imaging
NSiPM	Non-Simultaneous PET-MRI
OSEM	Ordered Subsets Estimation Method
PET	Positron Emission Tomography
PMT	Photomultiplier Tube
PSF	Point Spread Function
PVC	Partial Volume Correction
PVE	Partial Volume Effect
RES	Reticuloendothelial System
ROI	Region-Of-Interest
RR	Resolution Recovery
SFSRR	Structural and Functional Information for Resolution Recovery

SiPM	Simultaneous PET-MRI
SPM	Statistical Parametric Mapping
SPECT	Single Photon Emission Computed Tomography
SPIO	Superparamagnetic Iron Oxide
TE	Echo Time
TR	Repetition Time
USPIO	Ultrasmall Superparamagnetic Iron Oxide
WT	Wavelet Transform

List of Figures

2.1	Radioisotope decay. $N(0)$ is the initial number of radionuclides, τ is the exponential decay time constant and $T_{\frac{1}{2}}$ is the half-life of the radioactive isotope.	4
2.2	Schematic representation of a positron-electron annihilation.	5
2.3	Top: True event. Middle: Scatter coincidence. Bottom: Random event.	6
2.4	Detection of gamma-photons in PET.	7
2.5	Two possible geometries for PET-MRI systems. Left: NSiPM system where PET and MRI are axially displaced and the scans are acquired sequentially. Right: SiPm consists in placing the PET scanner within the MRI magnet such that PET and MRI scans are performed simultaneously.	11
2.6	The structure of a nanoparticle.	14
2.7	Schematic structure of a PET/MRI nanoprobe.	16
2.8	Point source of uniform activity (100 arbitrary units) in a nonradioactive background corresponds to a measured image in which part of the signal emanates and is seen outside the actual source. Maximum activity in measured image is reduced to 85.	17
2.9	In PET, the measured image results from the combination of spill-out and spill-in effects.	17
2.10	Representation of the SFSRR procedure.	24
3.1	Overview of SFSRR steps. [54]	27
3.2	Top to bottom, from left to right: True, PET, Segmented PET and Smoothed Segmented PET datasets.	29
3.3	Corrected PET data.	31
3.4	Mediso nanoScan PET/MRI scanner [74].	31
3.5	Solutions and corresponding tubes present in <i>Cucumis sativus</i>	33
3.6	Left: Original MRI data in SPM. Right: Original PET data in SPM.	35
3.7	Left: Original MRI data in SPM. Right: Flipped PET data in SPM.	36
3.8	Images load into AMIDE software. Top: MRI original data; Bottom: PET original data.	36
3.9	MRI and PET data after transformations.	38
3.10	Initial orientation of PET and MRI data.	39
3.11	MRI and PET data after flipping.	40
3.12	MRI and PET data after translation.	40

3.13	Top to bottom, from left to right: True, PET, Segmented PET and Smoothed Segmented PET datasets.	43
4.1	Simulated images (Top to bottom, from left to right): True data, PET data, Segmented PET data; (bottom, from left to right) Smoothed Segmented PET data and Corrected PET data obtained with SFSRR method.	46
4.2	Zoomed images. Left: PET data; Right: Corrected PET data. . .	47
4.3	Transverse and Coronal views of PET and Corrected PET datasets. . .	48
4.4	Line profiles from PET and Corrected PET datasets.	48
4.5	Maximum values in each slice of PET and Corrected PET datasets. . .	49
4.6	Mean values in each slice of PET and Corrected PET datasets. . .	50
4.7	Phantom data. Top to bottom, from left to right: PET and Corrected PET data 1 to 4.	51
4.8	Zoomed images of Corrected PET datasets for displaying the location of the negative values.	52
4.9	Tubes identification.	53
4.10	Solutions and corresponding tubes present in <i>Cucumis sativus</i> . . .	53
4.11	Maximum values in PET and Corrected PET datasets: Solution A - Tubes 1, 2, 6 and 5; Solution B - Tubes 8 and 7; Solution C - Tubes 3, 4, 9 and 10.	55
4.12	Mean values in PET and Corrected PET datasets: Solution A - Tubes 1, 2, 6 and 5; Solution B - Tubes 8 and 7; Solution C - Tubes 3, 4, 9 and 10.	56
4.13	Measured <i>Differences</i> for solutions A, B, C and water depending on the tube size and the smoothing values used.	59
4.14	<i>Differences</i> estimated for different nanoparticles solutions and smoothing values.	60
4.15	The relationship between image smoothing (FWHM in mm) and % difference of the tracer's uptake in the different tubes and solutions.	61

List of Tables

2.1	PET most common radioisotopes and corresponding $T_{\frac{1}{2}}$ values [4].	4
2.2	Properties of the most common PET radioisotopes [4, 20, 31].	8
2.3	Comparison between MRI and PET systems. [5, 8, 12, 26, 56, 88]	11
3.1	Intensity range for different SFSRR input data: PET, Segment PET and Smoothed PET.	30
3.2	Intensity range for Corrected data.	30
3.3	Nanoparticles and tracer concentrations evaluated in phantom data.	32
3.4	Parameters used in PET data reconstruction.	33
3.5	MRI data features.	34
3.6	PET data features.	34
3.7	Intensity range of PET and MRI in absence or not of a scaling factor.	34
3.8	MRI data centers.	37
3.9	PET data centers.	37
3.10	PET intensity values.	39
3.11	MRI intensity values.	39
3.12	MRI and PET new data features.	41
3.13	Input data and Corrected PET datasets 1 to 4, which correspond to the recovery data when using, respectively, $S1$ to $S6$ as <i>Smoothed Segmented PET data</i> .	44
3.14	Corrected PET datasets 1 to 4, which correspond to the recovery data when using, respectively, $S1$ to $S4$ as <i>Smoothed Segmented PET data</i> .	44
4.1	Intensity ranges of simulated data.	45
4.2	Minimum, maximum and mean values of the regions identified in PET and Corrected data.	45
4.3	Intensity ranges of PET and Corrected data. Corrected PET datasets differ in terms of the data used as <i>Smoothed Segmented PET data</i> in the SFSRR procedure: (i) in Corrected PET data 1 was $S1$; (ii) in Corrected PET data 2 was $S2$; (iii) in Corrected PET data 3 was $S3$ and (iv) in Corrected PET data 4 was $S4$.	50
4.4	Nanoparticles and tracer concentrations evaluated in phantom data.	53
A.1	Maximum values in PET and Corrected PET data and corresponding difference (%).	64

A.2	Mean values in PET and Corrected PET data and corresponding difference (%) between both datasets.	64
B.1	Maximum values in kBq/ml of the tubes present in PET and Corrected PET data.	65
B.2	Differences in the maximum values between different smoothing values, nanoparticles solutions and three sized tubes. Original PET data was used as reference, and deviations were calculated from this reference: $Difference = \left[\left(\frac{recovered\ value}{original\ value} \right) - 1 \right] \times 100\%$	66
B.3	Mean values in kBq/ml of the tubes present in PET and Corrected PET data.	67
B.4	Differences in the mean values between different smoothing values, nanoparticles solutions and three sized tubes. Original PET data was used as reference, and deviations were calculated from this reference: $Difference = \left[\left(\frac{recovered\ value}{original\ value} \right) - 1 \right] \times 100\%$	68

Chapter 1

Introduction

PET images are characterized by a low spatial resolution and lack of morphological information as a result of several factors: (i) positron range of the radioisotopes; (ii) scatter; (iii) attenuation; (iv) parallax error or radial elongation and (v) motion [4, 8, 73].

Partial Volume Correction (PVC) methodologies have been developed in order to minimize the aspects mentioned previously and improve PET images quality.

On the other hand, molecular imaging is a scientific area dedicated to the non-invasive study of biological processes. It assumes an important role in understanding the molecular abnormalities that are the basis of diseases and corresponding molecular alterations, guaranteeing an earlier disease characterisation and detection, as well as the evaluation of possible and important treatments.

Various imaging modalities - PET, MRI, SPECT (Single Photon Emission Computed Tomography), optical and ultrasound - can be used to assess the molecular targets. Although each imaging modality provides functional and/or anatomical information suitable for certain applications, all present intrinsic limitations. In this context, dual- or multi-modality molecular imaging arise from the combination of two or more imaging techniques based on the use of multi-modal probes, ensuring a better visualization of biological processes and acquiring more accurate data.

Bimodal nanoprobe have been developed, including nanoparticles that combine: (i) the high sensitivity of fluorescence imaging with the good contrast achieved with MRI; (ii) the high resolution of MRI with the high sensitivity and functional information characteristic of PET, obtaining data that contemplates both anatomy and functionality; (iii) high soft tissue contrast of MRI and high sensitivity of SPECT, however the latter one has a lower spatial resolution than PET [30].

Taking into account the low spatial resolution of PET images and the advantages of dual modality agents, this project aimed to evaluate the potential of combining PET/MRI nanoprobe and PVC procedures for improving the quality of PET images. More specifically, superparamagnetic iron oxide (SPIO) nanoparticles combined to ^{18}F radioisotope and the SFSRR PVC method were used as basis of the work developed.

SFSRR was selected as PVC method to apply in this project because it already showed promising results in PET brain studies comparing to other com-

mon PVC routines, more specifically van Cittert and Lucy-Richardson deconvolution techniques and also Geometric Transfer Matrix (GTM) approach.

The work developed consisted in: (i) performing a simulation study; (ii) acquiring PET and MRI datasets using a PET/MRI preclinical scanner; (iii) defining a processing protocol for phantom data and (iv) applying the SFSRR procedure to simulated and phantom data.

This thesis starts in Chapter 2 with a description of the basic concepts of PET, with special emphasis on the aspects that affect the quality of PET images (Section 2.1.3). Then, PET/MRI Systems, PET/MRI contrast agents and PVC aspects are described in detail.

In Chapter 3 is discussed the simulation study done and also the strategies followed for defining a processing approach suitable to phantom data. Finally, the PVC performed to simulated and phantom datasets is mentioned.

The results obtained and respective discussion are referred in Chapter 4.

Finally, conclusions and future perspectives are presented in Chapter 5.

Chapter 2

Theoretical Background

This chapter provides a background of the main topics that are covered in this thesis. Section 2.1 presents the physical concepts of PET, giving special emphasis to the factors that affect the quality of PET images. Then, PET/MRI systems are described in Section 2.2 and related with the use of PET/MRI nanoparticle agents in Section 2.3. The influence of PVES in PET and existing PVC approaches are discussed in Section 2.4. Finally, Section 2.5 mentions certain studies done in PET/MRI nanoprobe and PVC areas.

2.1 Positron Emission Tomography

2.1.1 Radionuclides and Positron Emission Decay

PET is a nuclear imaging technique that allows to assess functional processes by using a radiotracer which consists in a radioactive isotope associated to a molecule with specificity to a certain metabolic process.

PET radioisotopes, also known as radionuclides, emit positrons – positron decay – where a proton ρ^+ from the unstable radionuclide is converted into a neutron n by emitting a positron β^+ and a neutrino ν [4]:

$$\rho^+ \rightarrow n + \beta^+ + \nu \quad (2.1)$$

Assuming that N is the number of radioisotopes in the sample and α is the isotope decay constant, the decay probability per time unit or radioisotope's activity can be defined as [73]:

$$\frac{dN(t)}{dt} = -N(t)\alpha \quad (2.2)$$

where $\frac{dN(t)}{dt}$ is the radioisotope's activity that has Becquerel (Bq) as units and the negative sign represents the decrease in the number of atoms as time t increases.

The general solution of the differential Equation 2.2 for a time period $dt = t - t_0$ is [73]:

$$N(t) = N(t_0)e^{-\alpha(t-t_0)} = N(t_0)e^{-\frac{t-t_0}{\tau}} \quad (2.3)$$

where $N(t_0)$ is the initial number of atoms when $t = 0$.

The radioisotope decay obeys to an exponential function. It has $\tau = \frac{1}{\alpha}$ as time constant and $T_{\frac{1}{2}} = \ln 2 \tau = 0.69 \tau$ is the radioisotope half-life, which corresponds to the time required for 50% of the nuclei to disintegrate (Figure 2.1).

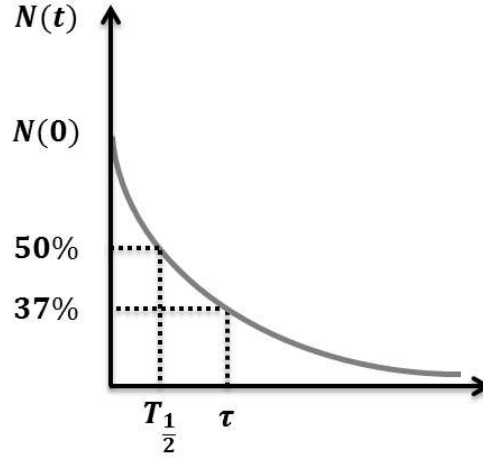


Figure 2.1: Radioisotope decay. $N(0)$ is the initial number of radionuclides, τ is the exponential decay time constant and $T_{\frac{1}{2}}$ is the half-life of the radioactive isotope.

The most common radionuclides used in PET are: Carbon-11, Nitrogen-13, Oxygen-15, Fluorine-18 and Gadolinium-68 (Table 2.1).

Isotopes	$T_{\frac{1}{2}}$ (min)
^{11}C	20.40
^{13}N	9.96
^{15}O	2.03
^{18}F	109.80
^{68}Ga	68.30

Table 2.1: PET most common radioisotopes and corresponding $T_{\frac{1}{2}}$ values [4].

The positron originated from the positron decay will suffer a decrease of its energy and change in its original path by interacting with other nuclei.

When the kinetic energy of the positron is sufficiently low, a positron-electron annihilation will occur, *i.e.*, the collision of a positron β^+ and an electron (e^-) will originate two gamma photons emitted in 180 degrees opposed directions and with an energy of 511 keV (Figure 2.2).

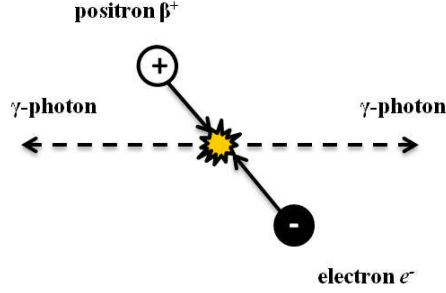


Figure 2.2: Schematic representation of a positron-electron annihilation.

Equation 2.4 describes the electron-positron annihilation process [8]:



The distance travelled by the positron until the annihilation occurs is called the positron range and it depends on the nature of the radioisotope used.

2.1.2 Detection of gamma photons

Inside the PET scanner, an array of detectors is displayed cylindrically around the object in order to detect the gamma photons from electron-positron annihilation events.

As mentioned previously, for a given annihilation event two gamma photons of 511 keV are emitted at almost 180 degrees to each other. In PET systems, two detectors are required to detect the γ -photons of the same pair. So, whenever two gamma photons are detected by distinct detectors within a timing window of around 1-10 nanoseconds, the detection is classified as a coincidence event. Thus, the radioactive source can be localized by defining a straight line between both detectors, designated as Line-Of-Response (LOR).

By estimating the intersection of all LORs, the location of the radiation source can be estimated more accurately.

There are three categories of coincidence events (Figure 2.3):

- True events - when both γ -photons originated from the same annihilation event are detected without suffering any interaction before detection;
- Scatter events - at least one of the detected photons underwent one or more Compton scatter events. If scattered photons are considered by the detector system, incorrect LORs will be defined;
- Random events - this occurs when two γ -photons detected are from distinct annihilation events and consequently a wrong LOR will be assigned. This happens when two radionuclides decay by chance within the same timing window.

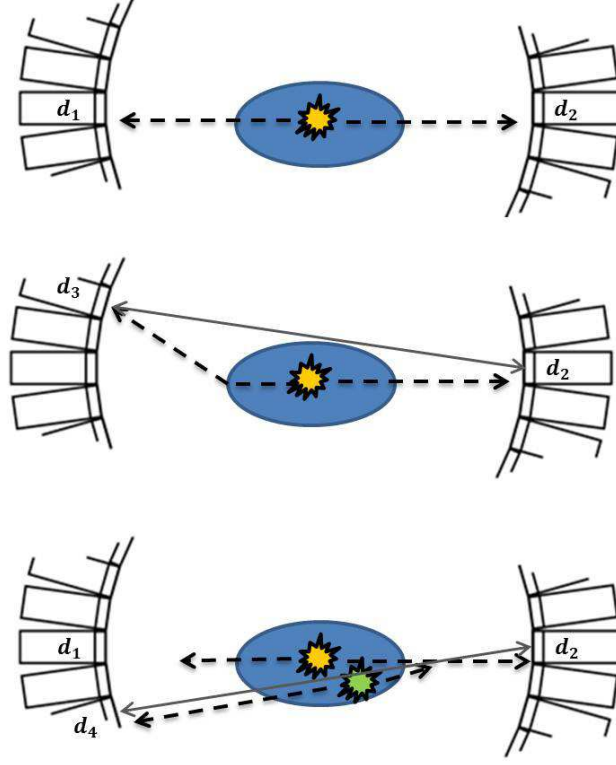


Figure 2.3: Top: True event. Middle: Scatter coincidence. Bottom: Random event.

If more than two γ -photons are detected by the PET system in the same timing window, the event will be rejected as it is not possible to determine which LOR is the correct one.

Assume that a certain LOR represents a s -axis and a point source is located in $s = a$ which emits $N(a)$ photons along this axis, as well as that two detectors are positioned, respectively, in $s = d_1$ and $s = d_2$.

According to a certain LOR, the gamma photons will pass through tissues with different characteristics and thicknesses which will translate into distinct *linear attenuation coefficients* μ . The value of μ indicates the fraction of photons that interact per unit distance ds of a certain material. It is characterized by the atomic number Z , density of the material and photons' energy.

The number of photons that interact within a small distance unit ds will depend on μ of the tissue and on the initial number of photons originated $N(a)$ [73]:

$$\frac{dN}{ds} = -N(a)\mu \quad (2.5)$$

The solution of Equation 2.5 is [73]:

$$N(s) = N(a)e^{-s\mu} \quad (2.6)$$

The different attenuation coefficients that exist for each small spatial portion ds must be considered when estimating the number of photons that reach each detector, so [73]:

$$N(d_1) = N(a)e^{-\int_a^{d_1} \mu(s)ds} \quad (2.7)$$

$$N(d_2) = N(a)e^{-\int_a^{d_2} \mu(s)ds} \quad (2.8)$$

As photons from the same annihilation event define independent trajectories, the detection probabilities can be multiplied [73]:

$$N(d_1, d_2) = N(a)e^{-\int_a^{d_1} \mu(s)ds} e^{-\int_a^{d_2} \mu(s)ds} = N(a)e^{-\int_{d_1}^{d_2} \mu(s)ds} \quad (2.9)$$

Figure 2.4 represents the detection of γ -photons in a PET camera.

Inside the detectors, scintillation crystals absorb the γ -photons via photoelectric absorption and photoelectrons are created.

During the photoelectrons displacement through the crystal, they will collide with other electrons present in the medium, originating light (scintillation) photons which are conducted to a photodetector, generally a photomultiplier tube (PMT). A PMT consists of a photocathode and a set of dynodes. Firstly, the photons hit the photocathode, releasing some electrons which then are accelerated towards the closest dynode. As the voltage becomes systematically higher with the distance, the electrons acquire higher speeds activating more additional electrons in every stage. Finally, the obtained signal is amplified by an amplifier located next to the PMT and an event is recorded.

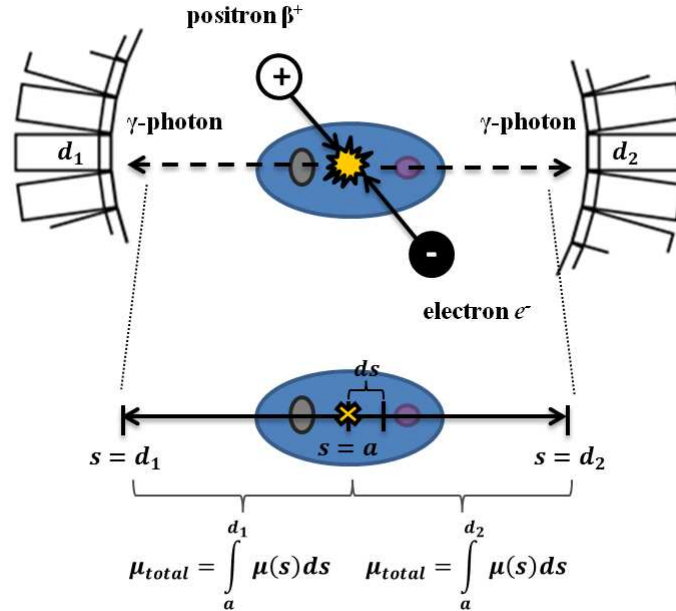


Figure 2.4: Detection of gamma-photons in PET.

2.1.3 Image Quality

PET images are affected by several factors which will be described in more detail below.

2.1.3.1 Positron Range

The main interest in PET is to infer the location of the decaying nucleus and not where the photon-producing event took place. However, the positron travels a finite distance before the annihilation occurs - positron range - which will lead to uncertainties in figuring out where the radionuclide nucleus is located. This aspect will affect the spatial resolution obtained in PET.

The positron range value depends on the nature of the radioisotope that originated the positron. For example, more energetic positron-emitting radionuclides have a higher positron range (Table 2.2), which will compromise more significantly the quality of PET images.

Isotopes	E_{max} positrons (MeV)	Mean range in water (mm)
^{11}C	0.959	1.1
^{13}N	1.197	1.5
^{15}O	1.738	2.5
^{18}F	0.633	0.6
^{68}Ga	1.898	2.9

Table 2.2: Properties of the most common PET radioisotopes [4, 20, 31].

2.1.3.2 Scatter

The γ -photons can suffer one or more Compton scatter events during their displacement. The resulting deflected photons have a lower energy and a change in their original trajectory.

The scattered photons have a lower energy than 511 keV, so the PET system can use this feature to suppress them as much as possible. However, some deflected photons are considered as coincidence events and consequently incoherences will occur.

Firstly, incorrect LORs will be defined which results in an overestimation of the tracer's concentration in certain regions, because counts that were not from these spatial locations will be contemplated.

As the accuracy of the quantitative measurements is affected, the contrast will also be compromised. More specifically, the contrast is estimated based on intensity differences detected between adjacent regions of an image and this is inferred based on the measured PET counts. If initially the detection is not precise, then the contrast will also be affected.

2.1.3.3 Attenuation

Attenuation in PET occurs mainly because of Compton scatter events and the chemical composition of tissues.

In Compton scatter events, the γ -photons experience a decrease in their energy.

Additionally, the energy of the photons can be attenuated based on differences in tissues characteristics and thicknesses (distinct attenuation coefficients).

In both cases, the photons from the same annihilation will have different energies, and so this pair will not be recognized as a coincidence event.

If several coincidence events are lost due to attenuation, then the number of PET counts from a certain region are underestimated.

This effect can be minimized by applying attenuation correction procedures which are performed based on transmission scans.

In a transmission scan, a source that emits radiation in a known range of energies (generally ^{68}Ge rod source or ^{137}Cs point source) is rotated around the patient. When the radiation passes through the patient body, its energy will be attenuated and is detected by the PET system, originating an image designated as transmission scan. The attenuation factors are estimated for each γ -photons pair, *i.e.*, each LOR. They can be calculated in accordance with Equation 2.10 [4, 73]:

$$\frac{N_0}{N} = e^{-\int_{d_1}^{d_2} \mu(s) ds} \quad (2.10)$$

where N_0 is the number of photons detected in the emission scan between two detectors located in $s = d_1$ and $s = d_2$, N is the number of photons counted between the same detectors in the transmission scan and μ is the linear attenuation coefficient.

The transmission data can be considered during the reconstruction of the emission data, improving its quality.

Another attenuation methodology is available in PET/CT scanners. PET data is acquired and then a CT scan is performed and used to create a 511 keV attenuation map. This approach can introduce artifacts if PET and CT data are not correctly registered.

Finally, nowadays MRI guided attenuation correction procedures are also available, however they are not as efficient as CT based procedures. This occurs because MRI signal is not electron density dependent which complicates the determination and location of the major attenuating structures. As a consequence, it is more challenging converting MRI data into attenuation maps than using CT images.

2.1.3.4 Parallax error or Radial elongation

The gamma photons that strike detectors located in the gantry edges will interact with the scintillation crystal according to a certain angular divergence. Therefore, there is less material to stop the gamma radiation, and so the photon will suffer a spillover of its trajectory and will interact with the adjacent crystal. This aspect compromises the quality of PET images as the radioactivity detect near gantry edges has worst resolution (wider Full-Width-Half-Maximum - FWHM) than in the center. The spatial resolution is expressed in terms of FWHM which corresponds to the minimum distance that two point sources positioned very close are seen as separate in an imaging system.

2.1.3.5 Motion

PET scans last longer than other imaging modalities, therefore the effect of motion in PET image quality is more significant.

Motion artifacts can occur due to changes in patient's position during the scan, respiration, cardiac motion, peristalsis or bladder filling. In order to overcome these aspects, motion correction procedures need be used which efficiency decreases significantly in presence of intense tissue-movement.

2.2 PET/MRI Systems

PET and SPECT have a high sensitivity to assess metabolic pathways in the picomolar range by using radiotracers. However, these nuclear imaging techniques have a low spatial resolution, compromising the accurate spatial detection of the decaying nuclei locations. In contrast, CT and MRI have a good anatomical contrast but a low sensitivity.

As a consequence, in order to ensure a proper diagnosis and/or treatment planing, generally SPECT or PET images are combined with CT or MRI data through registration procedures.

In this context, since the late 1990's medical devices that integrate different imaging modalities in the same system have been developed which are designated as *Hybrid imaging devices* [8]. Thus, these systems combine the advantages of each imaging technique. At the present, there are three types of hybrid devices: SPECT/CT; PET/CT and PET/MRI.

The first hybrid imaging equipment created was SPECT/CT in 1998 followed by PET/CT in 2000. More recently, PET/MRI systems have been developed [8].

Over the last years, PET/MRI systems have achieved a great relevance in comparison to PET/CT scanners due to several aspects.

On the one hand, MRI images have a higher contrast and greater spatial resolution than CT, as well as this modality provides a wider range of information - structural, functional, diffusion, spectroscopy, angiography and perfusion. Also, MRI does not expose the patient to additional radiation in contrast to what occurs in PET/CT scanners. However, attenuation correction procedures are more efficient when using CT data as basis than MRI images.

On the other hand, PET allows the study of metabolic processes with high accuracy and sensitivity, nevertheless its spatial resolution is low due to positron range, scatter, attenuation and motion (2.1.3).

Table 2.3 summarizes the advantages and limitations of MRI and PET.

Modality	Spatial resolution	Advantages	Limitations
MRI	Tens of micrometers (preclinical systems) 1 mm (clinical systems)	High resolution Good contrast Physiological and anatomical details	Low sensitivity ($10^{-3} - 10^{-5} mol/l$) High cost Artifacts due to metallic devices in patients
PET	1 mm (preclinical scanners) 4-6 mm (whole-body systems)	Study of metabolic processes High sensitivity ($10^{-11} - 10^{-12} mol/l$)	Radiation High cost Lack of anatomical information

Table 2.3: Comparison between MRI and PET systems. [5, 8, 12, 26, 56, 88]

Based on the features mentioned in Table 2.3 is possible to conclude that MRI and PET are really distinctive in terms of resolution, sensitivity and type of information provided. As a consequence, these imaging techniques are commonly combined, either in separate scanners or in PET-MRI systems, in order to obtain more accurate information.

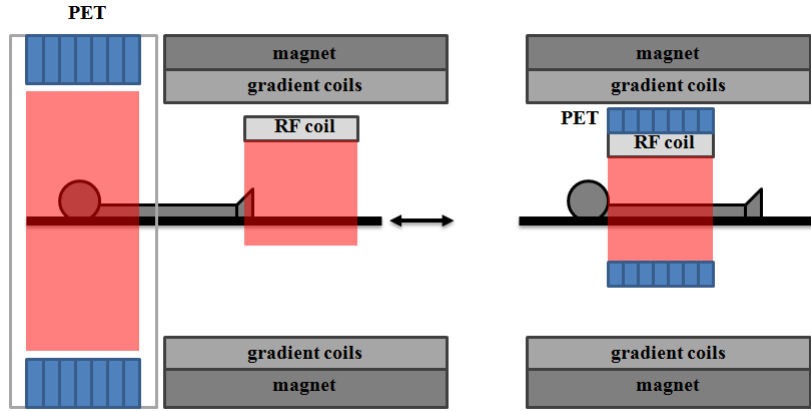


Figure 2.5: Two possible geometries for PET-MRI systems. Left: NSiPM system where PET and MRI are axially displaced and the scans are acquired sequentially. Right: SiPM consists in placing the PET scanner within the MRI magnet such that PET and MRI scans are performed simultaneously.

There are two types of PET-MRI systems:

- Non-Simultaneous PET-MRI (NSiPM) – in this system the patient lies on the bed that moves automatically and alternatively between PET and MRI scanners. Images are sequentially acquired, *i.e.*, the data from both imaging modalities is acquired in distinct time periods. Thus, a registra-

tion procedure must be carried out so that PET and MRI data can be analysed together;

- Simultaneous PET-MRI (SiPM) – allows acquiring simultaneously PET and MRI images. Therefore, it will be possible to overcome the coregistration errors induced by organ and/or patient motion as real-time MR and PET images are available. This approach assumes quite relevance in biological studies where the radiotracers response is highly dynamic and time dependent.

Regarding the disadvantages of NSiPM, in this technology PET and MRI images are acquired separately and then registered. The registration is performed based on image data contents (e.g., landmarks) or external markers existing in the images subjected to registration. Registration gives good results in the brain, but becomes more difficult for other parts of the body, which result from the change in patient's position in the scanner bed, respiration, cardiac motion, peristalsis or bladder filling. In order to overcome these aspects, deformable (non-rigid) image registration techniques can be used, but their efficiency decreases significantly in the presence of severe tissue-movement.

Another limitation of NSiPM system is that during the acquisition of images from one modality, the other scanner must remain idle. As a consequence, a higher scanning time is required which is not ideal for assessing the radiotracer's concentration when it is highly variable in terms of time and biodistribution.

On the other hand, SiPM system faces several problems which are:

- Electromagnetic interference due to MRI magnetic radiofrequency pulses and gradient coils, or because of PET electronic system that has radiofrequency emitting components which can interfere with the MRI system;
- Effect of MRI main magnetic field on PET detectors, more specifically, classic photomultiplier tubes used for detecting gamma photons cannot operate properly in the presence of a magnetic field;
- Induction of eddy currents – the MRI scanner has a permanent magnetic field, however during the pulse sequences there is a rapid variation of magnetic field gradients. As a result, the conductive structures are subjected to changes in the magnetic field and electric currents can be induced in PET conductive materials;
- The increase of vibrations and temperature due to MRI sequences will affect the ideal conditions for PET imaging;
- Susceptibility artefacts occur when the PET system is located inside the MRI magnet.

Taking into account SiPM limitations, the design of PET electronic components has to be adapted to MRI magnetic features in order to merge these two imaging techniques in the same unit.

2.3 Contrast Agents

2.3.1 Nanoparticles

Iron oxide nanoparticles generally consist of three parts (Figure 2.6):

- **core** - metallic nature which is responsible for enhancing the MRI signal;
- **shell** - confers biocompatibility to nanoparticles in order to avoid their degradation and initiate an immune response;
- **bioactive materials** - elements associated to nanoparticles' surface for targeting purposes.

Nanoparticulate materials have achieved a great importance in molecular imaging for several reasons:

- Internal volume – can be used for transporting and delivering imaging and therapeutic agents;
- Large surface area – nanoparticles can be associated to a high number and variety of active elements, improving physical and/or chemical interactions and reactivity;
- Non-invasive approach for monitoring biological processes, in terms of drug delivery, response to therapeutic agents and imaging detection;
- High sensitivity achieved when combining them with antibodies and other targeting agents;
- Multimodal imaging – conjugation with different probes for being detectable by distinct imaging modalities.

Based on these features, nanoparticles assume a big relevance in imaging as they can transport and deliver a big quantity of contrast agents until the target area – high sensitivity – as well as they can be associated to different probes in order to be detectable by distinct imaging modalities.

Also, nanoparticles face several challenges which are:

- High tissue-selectivity without significant intervention of the RES (reticuloendothelial system);
- Non-toxicity;
- Full clearance from the system;
- Non-immunogenicity.

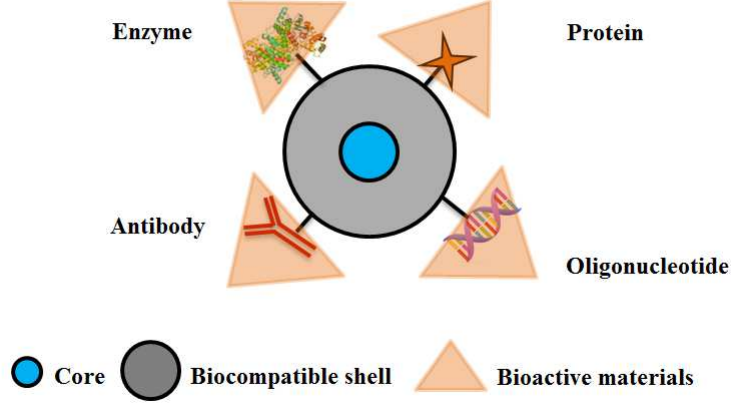


Figure 2.6: The structure of a nanoparticle.

2.3.2 MRI contrast agents

MRI reveals the anatomical details with good spatial resolution and contrast, however sometimes it is a challenge to distinguish certain tissues, for instance, normal and diseased tissues, due to small differences in their specific relaxation times.

This aspect can be minimized by using MRI contrast agents which can be categorized in: T_1 contrast agents and T_2 contrast agents.

2.3.2.1 T_1 contrast agents

T_1 contrast agents are based on paramagnetic atoms and are responsible for shortening the T_1 relaxation time of protons located nearby these agents by exciting protons from high-energy to low-energy states. This will lead to a hypersignal in their locations which results in brighter areas in T_1 -weighted images.

Magnetization of paramagnetic complexes only occurs in presence of an external magnetic field and it is directly related with the number of paramagnetic ions present in the target tissue. The most common paramagnetic agents used are: (i) Gadolinium (Gd^{3+}) and (ii) Manganese (Mn^{2+}).

2.3.2.2 T_2 contrast agents

T_2 contrast agents are based on superparamagnetic compounds that consist of iron oxide nanocrystals, usually magnetite Fe_3O_4 or maghemite $\gamma-Fe_2O_3$, and they can be classified in:

- Superparamagnetic iron oxide (SPIO) - approximately 60-150 nm;
- Ultrasmall superparamagnetic iron oxide (USPIO) - approximately 10-40 nm [11, 78].

Superparamagnetic compounds can be magnetized by an external field as paramagnets, however they have a larger magnetic susceptibility. More specifically, in paramagnetic materials each atom is influenced independently by the magnetic field while in superparamagnetic compounds the entire magnetic moments of the atoms tend to align along the external magnetic field, which leads to a higher strengthening of the magnetic field. When the external magnetic field disappears, their magnetization decreases to zero as there are fluctuations in the magnetization direction of individual atoms.

Based on the previous property, superparamagnets show a strong magnetization, creating local field inhomogeneities. This will lead to the decrease of T_2 and T_2^* relaxation times of the tissues where superparamagnets are located through the loss of coherence of the local protons, resulting in a hypo-intensity (dark contrast) of these areas in T_2 -weighted images.

2.3.3 PET/MRI nanoparticle agents

MRI is one imaging technique that has good spatial resolution and tissue contrast, however it has low sensitivity. When using nanoparticle agents in MRI, there is an improvement in the MR signal, resulting in images with a better spatial resolution and contrast. This assumes a great relevance in diagnostic and treatment purposes.

On the other hand, radiolabeled nanoprobe in PET allow the study of biological mechanisms with high sensitivity and accuracy. However, a major limitation of PET is that it cannot provide anatomical information, preventing the precise spatial detection of the imaging agents.

Since each imaging modality cannot provide all types of required information, the development of new hybrid devices that combine different imaging techniques has been focus of research.

All these aspects led to the development of multimodal nanoparticle agents which consist in nanocarriers associated to probes, enabling their detection by more than one imaging technique. Therefore, it is possible to combine the advantages of distinct modalities, and additionally improve data acquisition and guarantee a better non-invasive diagnosis and treatment.

Generally, PET/MRI nanoparticle agents have three components:

- core;
- targeting molecule - that has high affinity towards the biological target;
- radiotracer group - can be directly linked to the nanoparticle surface or through a spacer group, which can be a hydrocarbon chain, peptide sequence or a poly-ethyleneglycol (PEG) linker.

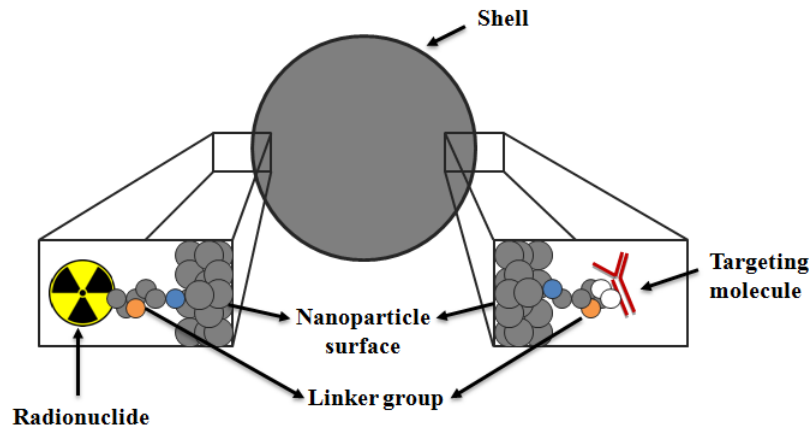


Figure 2.7: Schematic structure of a PET/MRI nanoprobe.

2.4 Partial Volume Correction (PVC)

2.4.1 Partial Volume Effects

Positron emission faces several problems as explained previously in Section 2.1.3:

- Positron range;
- Scatter;
- Attenuation;
- Parallax error or radial elongation;
- Motion.

Due to these aspects, partial volume effects (PVEs) can occur which are characterized by loss of detail and/or apparent activity in small objects or regions at spatial and/or time levels, compromising the anatomical or functional information obtained.

There are three different categories of PVEs:

- Spill-over;
- Sampling effect;
- Temporal aspects.

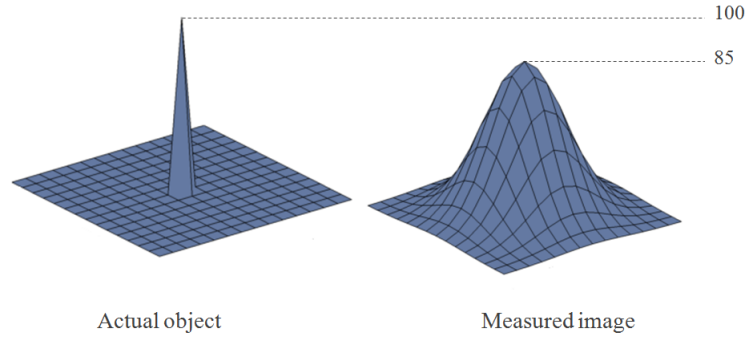


Figure 2.8: Point source of uniform activity (100 arbitrary units) in a nonradioactive background corresponds to a measured image in which part of the signal emanates and is seen outside the actual source. Maximum activity in measured image is reduced to 85.

Spill-over generally occurs when the object size is two or three times smaller than the FWHM of the PET image [72]. Therefore, smaller objects tend to be more affected by PVEs, resulting in a more significant spill-over of the tracer's distribution in the object:

$$\text{Spill-over} \Rightarrow \text{Object size} < (2 \text{ or } 3) \times \text{FWHM} \quad (2.11)$$

There are two types of spill-over:

- *Spill-out* - the radioactivity detected on the region-of-interest (ROI) is higher than in the adjacent areas, which spreads into the neighbour tissues. Consequently, there is an underestimation of the tracer's uptake;
- *Spill-in* - when the surrounding areas have higher activity than the ROI, their activity will spill into the ROI. Thus, the uptake will be overestimated.

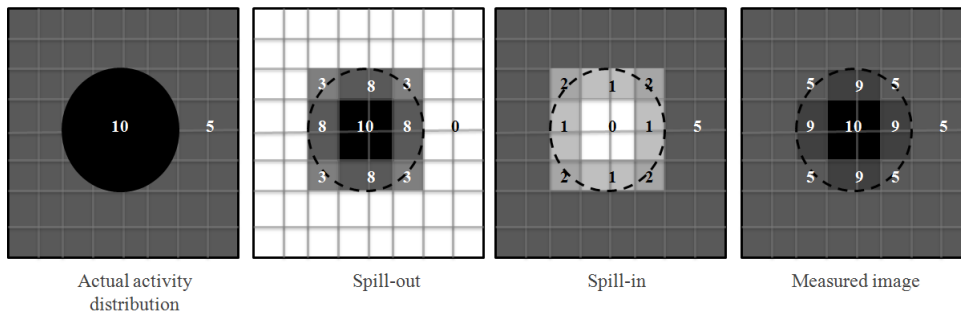


Figure 2.9: In PET, the measured image results from the combination of spill-out and spill-in effects.

Image sampling, also known as tissue-fraction effect, can contribute to PVEs when within each voxel there are different tissue types which might have distinct tracer concentrations. In this case, the value given to the voxel with mixed tissues is the mean activity, which does not describe the true tracer’s distribution.

Additional PVEs can arise due to temporal factors:

- Blurring because of the heartbeat, respiration or patient motion;
- In dynamic studies, the change in the radiotracer’s activity and distribution over time.

All these factors affect PET images both qualitatively and quantitatively.

2.4.2 PVC procedures

In order to minimize the impact of PVEs in PET images, several strategies have been proposed – Partial Volume Correction (PVC) methodologies - that aim to restore the true activity distribution of the object.

The tissue-fraction effect just can be improved if anatomical information, CT or MRI, are included during PVC.

In terms of the PVC methods available, they can be categorized in:

- Reconstruction methods;
- Postreconstruction methods.

Each category includes region-of-interest (ROI) and voxel-based approaches. ROI methods estimate the tracer’s uptake in each region and then its original value is modified according to the recovery model applied. These approaches do not originate PVE-corrected images, but instead change the corrected regional activity values. Therefore, they are only suitable for quantification purposes and not for visual analysis [72]. On the other hand, voxel-based methodologies produce PVE-corrected images which are characterized for being more mathematically complex and rely on the use of structural images.

In addition, some methods are performed just based on the data available, while others also consider anatomical information.

It is important to highlight that there is not an optimal PVC method for all possible PVEs. It depends on the intended application of the acquired PET images [21]. So, different types of PVC techniques are described in this section.

2.4.2.1 Post-reconstruction methods

Post-reconstruction PVC methods are applied directly in the reconstructed image.

Iterative Deconvolution methods

Iterative deconvolution methods are data-driven and involve performing multiple comparisons between the measured data values and the values estimated according to the deconvolution model, in order to estimate the true tracer’s activity.

Deconvolution procedures do not need homogeneity assumptions which consider that the estimation of the radiotracer's uptake in a certain structure or region is independent from others' structures activity, which it is not true in all cases. On the other hand, deconvolution approaches have difficulty in controlling noise amplification, compromising the efficiency of the PVC performed.

Noise correction can be achieved during deconvolution by including high resolution data and regularisation.

Two common deconvolution techniques are:

- Richardson-Lucy algorithm - it is a Bayesian approach where the noise present in the data is assumed to obey to a Poisson distribution [75,79];
- van Cittert method - aims to estimate the true tracer's activity that equals the measured distribution and the blurred version (obtained by iteratively deconvolving an image with a known PSF - Point Spread Function) based on the application of a least-square approach [79].

Inclusion of anatomical information

Another methodology available consists in combining the high frequency information of structural images, CT or MRI, with PET functional data. This will result in an improvement of the contrast and anatomical details in PET images.

For this purpose, PET emission data and anatomical images are registered, so it is possible to know the accurate location of the different structures and use this information for correcting the tracer's distribution.

However, the effectiveness of these methodologies depends on: (i) PET and structural images' registration and (i) segmentation of the anatomical image, if required.

Some methods included in this category are:

- Geometric Transfer Matrix (GTM) [59]

GTM obeys to the following steps:

1. A MRI image is segmented into multiple regions;
 2. In each ROI, a regional spread function is estimated and a blurred version is created which just contemplates the activity in this area. Each ROI is assumed to have uniform activity, so it is valid to describe the regional tracer uptake by the mean value;
 3. It is verified which ROIs have higher or lower activities;
 4. The true activity distribution is computed based on the information obtained in 2) and 3).
- Boussion et al [9] - involves the use of the wavelet transform for extracting high frequency information from CT or MRI images. Then, it is estimated the existence or absence of correlation between structural and PET images in different regions. If there is correlation in a specific region, then the high frequency components of the anatomical image are incorporated in PET image, if not PVC is not performed in this ROI.

- SFSRR (Structural and functional Information for Resolution Recovery) - was developed by Shidahara et al [68]. It is a modified approach of Boussion et al [9] method, however in this case a brain atlas is used to segment the anatomical prior. This procedure was used in this project and a full description is given in Section 2.4.5.

2.4.2.2 Reconstruction-based methods

An alternative is to perform PVC during the reconstruction procedure. This strategy has two main benefits: (i) modelling scanner resolution is easier in projection data than in the image domain and (ii) the noise present in the projection domain obeys to a Poisson distribution while in the image space does not assume a particular behaviour/distribution.

As a result, there is a minimization of PVEs in magnitude and a better control of noise, however quantitative correction is limited by the prevalence of some residual PVEs which might be difficult to estimate due to the non-linearity of reconstruction methods.

Resolution Recovery

Simulations related with the PSF of the imaging system aim to explore the spatially-variance between PET tracer's biodistribution and the measured counts.

The derived/modeled PSF can be considered in the system's matrix which then is reconstructed, in order to correct physical factors such as scatter, attenuation and motion, as well as to improve the accuracy of the quantitative measurements.

The quantitative correction using this approach is limited by the prevalence of some residual PVEs as they are difficult to estimate due to the non-linearity of some reconstruction methods.

One example of a resolution recovery method was developed by Comtat et al [13] in 2008, where the system matrix includes the measured projection data and a modelled space-invariant Gaussian PSF that covers the blurring effects of the PET scanner. Then, the system matrix was reconstructed by using OSEM (Ordered Subsets Estimation Method) and the results obtained showed that a higher tracer's uptake was detected in small structures when this model was applied.

Anatomical priors

Structural information can be associated during the image reconstruction step and their main goal is to suppress noise.

Usually anatomical priors are smoothed so that is possible to minimize the noise present in the data and emphasize the important details in images.

In terms of the different procedures that combine anatomical priors to functional data, some examples are:

- Sastry and Carson (1997) [62] created a maximum a posteriori (MAP) algorithm which basis is a MRI segmented image for classifying tissues

according to their composition. Then, each region is associated to the corresponding activity;

- Bowsher et al (2004) [10] – first of all the structural images are subjected to smoothing for reducing any existing variations between voxels with similar MRI signals. As a result, the filtering step will emphasize voxels that differ anatomically and thus more accurate results are obtained when using anatomical data for SPCT or PET images resolution recovery;

2.4.3 Efficiency of PVC procedures

The efficiency of PVC procedures is influenced by the aspects that will be discussed below.

2.4.3.1 Image Registration

Certain PVC methods use *a priori* anatomical data for improving the resolution of PET images. In this case, the efficiency of the PVC performed is partially dependent on the accurate registration between structural and functional images.

Image registration errors will affect the new PET counts estimations, compromising the veracity of the results obtained.

2.4.3.2 Image segmentation

Additionally, PVC can be affected by image segmentation if the PVC procedure requires any segmented data.

Incoherences in the segmentation step occur at region level, while misregistration errors influence the entire image.

2.4.3.3 Tissue inhomogeneity

The structural and functional features of the tissues can influence the PVC methods.

Depending on the conditions that tissues are subjected, their activity can vary. Also, tissues' components may not be uniformly distributed.

Thus, the tracer's distribution in a region or tissue can be heterogeneous and consequently the homogeneity hypothesis which several PVC methods are based on will compromise the results obtained.

One possible solution for this aspect consists in performing inhomogeneity tests - Krylov subspace iteration - in order to evaluate if it is viable to assume that a certain tissue has an homogeneous tracer's distribution in all its extension. The limitation of this test is that it just gives accurate results when associated to a noise model [60].

2.4.3.4 Gibbs artifacts

Gibbs artifacts are characterized by the existence of a brilliant or dark lines in the boundary of tissues or areas with distinct tracer concentrations.

In certain occasions PET reconstructed images show Gibbs artifacts which can occur due to:

- Information loss resulting from the limitations of the detector system;
- Insufficient data as the voxels dimensions are too large.

2.4.4 Applications of PVC

PET images are influenced by several degrading factors, inducing PVEs that will affect the accuracy of the quantitative measurements performed. Thus, PVC is relevant for providing true functional information about physiological and biological processes. This information might be applied on tumor metabolism quantification, cerebral blood flow, myocardial perfusion, glucose metabolism and neuroreceptor binding, however PVC is not a common routine in clinical practice [60].

The main applications of PVC have been: brain imaging; cardiology and tumor imaging.

Neurodegenerative diseases, such as Alzheimer’s disease, are characterized by atrophic changes, particularly in cortical grey matter. Atrophy causes the thinning of cortical structures, which in turn become more susceptible to PVEs and so the use of PVC procedures guarantee a more accurate visual of any anatomical changes.

PVC has also contributed to clarify and/or support important findings in brain PET imaging. In Alzheimer’s disease, the decrease in glucose metabolism detected does not correspond to an artefact due to the existence of a bigger CSF (Cerebrospinal Fluid) space, but in reality it reflects a metabolic alteration resulting from this pathology. Additionally, PVC has highlighted that there is a decrease in dopa-decarboxylase activity in Parkinson’s pathology [60].

In terms of cardiology, spillover of the activity from the blood pool towards the myocardium wall is a common problem in myocardium studies. In this case, PVC procedures can be used for guaranteeing more accurate quantitative and flow measurements in myocardial perfusion imaging. Also, the possibility of correlating PET data with structural images (CT or MR) during PVC improves the spatial discrimination of the activity uptake detected in blood’s pool and myocardium, as well as it helps to differentiate between necrotic and health myocardium tissues in case of cardiac events, for example myocardial infarction [60].

Another focus of research in PVC is tumor imaging. PVC approaches are used to improve lesions’ uptake in order to accurately delineating the metabolic parts of a tumor and also to distinguish between healthy and cancerous cells [60].

2.4.5 Structural and Functional Information for Resolution Recovery (SFSRR)

In this project, the PVC method used was developed by Shidahara et al – SFSRR (Structural and functional Information for Resolution Recovery) – and consists in a wavelet-based resolution recovery method [32, 67, 68].

SFSRR is based on the Wavelet Transform (WT) which decomposes a signal $f(x)$ as a sum of translations (k) and dilations (j) into the spatio-frequency domain. For achieving this objective, Multiresolution analysis (MRA) is used which decomposes the signal $f(x)$ through a high-pass filter ψ and a low-pass filter φ [67, 68]:

$$f(x) = \sum_k \sum_{j=1}^J d_j(k) \cdot \psi_{j,k}(x) + \sum_k C_j(k) \cdot \varphi_{j,k}(x) \quad (2.12)$$

The elements of Equation 2.12 are:

- First and second terms represent, respectively, the high and low (residual) frequency components of the image;
- $d_j(k)$ are the wavelet coefficients estimated by doing the inner (scalar) product between the original signal and $\psi_{j,k}$ orthonormal basis elements. As a consequence, the numeric coefficients that characterize each element of the original signal situated at the position k and in the j frequency band (resolution level) are obtained;
- The high-pass function ψ is an orthonormal wavelet - Hilbert basis - as it can be described by a family of functions $\psi_{j,k} : j, k \in \mathbb{Z}$ (orthonormal basis elements) that characterize the multiples translations and dilations of ψ ;
- $C_j(k)$ are the scaling coefficients that represent the low frequency image elements (residual).

The resolution recovery of PET images is done by using *a priori* anatomical data which can be a CT or MRI image. The high frequency information present in the structural data compensates the low morphological details of PET, guaranteeing an improvement in the existing anatomical aspects without affecting the functional data.

The input data of this approach are:

- *PET data* - original PET data;
- *Segmented PET data* - the MRI or CT image is segmented and then for each ROI is calculated the corresponding PET mean value;
- *Smoothed Segmented PET data* - Segmented PET data is smoothed by applying a Gaussian filter.

SFSRR works according to three steps.

Firstly, *PET*, *Segmented PET* and *Smoothed Segmented PET data* are decomposed by applying Equation 2.12. Consequently, wavelet coefficients for each input data are estimated, respectively, d_j^{PET} , d_j^{ana} and d_j^{anas} .

Secondly, a weighted correlation of the wavelet coefficients is performed based on three scaling factors [32, 67, 68]:

$$d_j^{corr}(k, q) = \beta_j(\gamma_j(\alpha_j \cdot d_j^{ana}(k, q)) + (1 - \gamma_j)d_j^{PET}(k, q)) \quad (2.13)$$

where α_j , γ_j and β_j are the scaling parameters; q represents the quadrants (directions) in which the image was decomposed.

Factor α_j contemplates the intensity variances between PET and Segmented PET data.

The second parameter γ_j evaluates if it is necessary to include structural information to the current PET data.

The recovery coefficient β_j compares any spatial resolution differences between *Segmented PET* and *Smoothed Segmented PET* images. It is calculated by doing the ratio between the wavelet coefficients from *Segmented PET* image d_j^{ana} and *Smoothed Segmented PET* image d_j^{anas} (smoothed with a 3D Gaussian filter in order to match PET's resolution).

Finally, the estimated $d_j^{corr}(k, q)$ coefficients are applied to the original PET image, resulting in an enhancement of its quality.

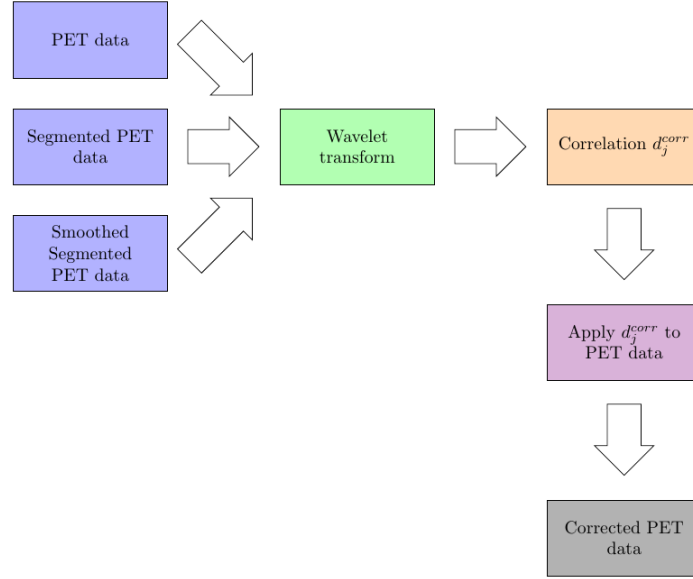


Figure 2.10: Representation of the SFSRR procedure.

2.5 PET/MRI nanoprobe studies

2.5.1 PET/MRI nanoprobe

In the last years, PET/MRI nanoprobe have become relevant because PET and MRI are quite complementary techniques. PET has a really good sensitivity for studying metabolic processes, but faces challenges in terms of spatial resolution and lack of morphological information. This can be overcome by synergistically combining PET to MRI which provides images with high-resolution and anatomical information. Additionally, the nano-nature of these probes allows to explore the existing internal volume for transporting and delivering imaging and therapeutic substances to specific targets. Also, nanoparticles' large surface area gives the possibility of combining a wide variety of substances for monitoring biological processes, imaging detection and evaluation of drug delivery.

Two studies have shown that nanoparticles are good contrast agents for detecting lymph node metastases when using PET and MRI techniques, which were performed by Choi et al (2008) [69] and Rafa et al (2011) [15].

Another area focus of interest in PET/MRI nanoprobe is cancer imaging. Certain tumor cells have integrins in their membranes which are proteins com-

posed of two glycoprotein chains called alpha α and β subunits. These integrins expressed by tumour cells stimulate cell multiplication and migration. Based on this aspect two scientific groups, Lee and coworkers (2008) [33] and Yang et al (2011) [86], developed dual modality nanoprobe for evaluating their efficiency in targeting in vivo tumor integrin $\alpha_v\beta_3$ expression cells.

Another type of tumor explored in PET/MRI nanoagents development was glioblastoma, which is the most common brain tumor in humans. It affects the glial cells present in the brain and spinal cord. Just one study involving PET/MRI nanoparticles and glioblastomas was done by Luo et al (2012) [41].

Pancreatic cancer was also considered in PET/MRI nanoprobe development by Locatelli et al (2012) [38], and more recently Kim et al [51] created a colon tumor-targeting nanoagent in 2013.

Also, PET-MRI nanoprobe have been used in macrophage imaging for diagnosing atherosclerosis. This disease is characterized by the formation of plaques within the arteries walls, resulting from the accumulation of fatty substances, such as cholesterol and triglyceride, and calcium. The normal blood circulation is affected, creating a thrombus and a chronic inflammatory response in the affected area, activating macrophages and white blood cells towards the atherosclerotic plaque. Therefore, in 2010 Jarret et al [29] and also by the year of 2013 Majmudar and coworkers [45] created PET/MRI nanocarriers that target monocytes and/or macrophages present in atherosclerotic plaques.

Finally, two more groups, Glaus and coworkers (2010) [23] and Sharma et al (2013) [66] developed iron-oxide nanoparticles associated to PET isotopes in order to evaluate their ability for being PET/MRI dual probes, *i.e.*, verify any changes in PET and MRI signals and respective activity uptake and/or contrast in images.

2.5.2 PET/MRI nanoprobe and PVC

The study that lead to this project was done by Rosales et al [15] in 2011. It consisted in developing a novel multimodal imaging agent with an iron oxide core - MRI probe Endorem/Feridex (chemical formula Fe_3O_4) - associated to ^{124}Cu isotope. PET-MR imaging studies were performed in a mouse to assess the efficiency of these nanoagents for being taken by lymph nodes. MRI images showed a decrease in T_2^* contrast in regions where there was an accumulation of nanoparticles, more specifically in popliteal and iliac lymph nodes, which corresponded to a higher tracer's uptake in PET images.

Until the present date no work has explored the potential of combining PET/MRI nanoprobe and PVC procedures in order to improve the quality of PET images, so this project is the first one developed on this area.

Chapter 3

Materials and Methods

The materials and methods used in this thesis are referred in this chapter.

Firstly, the SFSRR procedure and its application to PET brain studies are explained in Section 3.1.

Then, the method used for generating simulated data and corresponding PVC performed are discussed in Section 3.2.

Finally, phantom data is described in detail in Section 3.3, giving emphasis to the PET/MRI system used to acquire the data (Section 3.3.1), the experiments done for defining an image processing protocol suitable for this dataset (Sections 3.3.3 and 3.3.4) and the PVC carried out in phantom data (Section 3.3.5).

3.1 SFSRR procedure - original processing protocol

SFSRR is a PVC procedure developed for PET brain studies. The program has a graphical user interface and works according to five steps:

- Initialization;
- Co-registration;
- Segmentation;
- PET Brain Masking;
- PVC.

Firstly, original PET and MRI images are considered as input files in *Initialization* step. If both have distinct orientations, then flipping of data can be performed. The output file(s) are automatically contemplated in the following step.

In *Co-registration* step, PET image is registered into MRI native space.

Then, in order to perform the *Segmentation* step, a human brain atlas - *Hammers^{smith} atlas* - is considered as an additional input [24]. *Hammers^{smith} atlas* has 83 ROIs (regions-of-interest) that characterize distinct brain structures. *Segmentation* involves:

1. Co-registration of the *Hammers^{smith}* atlas into MRI native space;
2. Segmentation of the MRI image;
3. For each anatomical region is assigned the regional PET mean value.

As a result, a *Segmented PET atlas* is created which contemplates the anatomical features of the original MRI image and the average PET counts for each ROI in co-registered PET data.

In *Masking* step, a brain mask is applied to the original PET image so that the counts located outside the brain are set to zero. The resulting file is called *Masked PET data*.

Finally, *Segmented PET atlas* and *Masked PET data* are the input files of the *PVC* step which requires:

1. Reslice *Segmented PET atlas* into PET space;
2. *Segmented PET atlas* is smoothed by using a Gaussian filter and a new dataset named *Smoothed Segmented PET data* is created;
3. PVC is performed taking into account *Masked PET data*, *Segmented PET atlas* and *Smoothed Segmented PET data*.

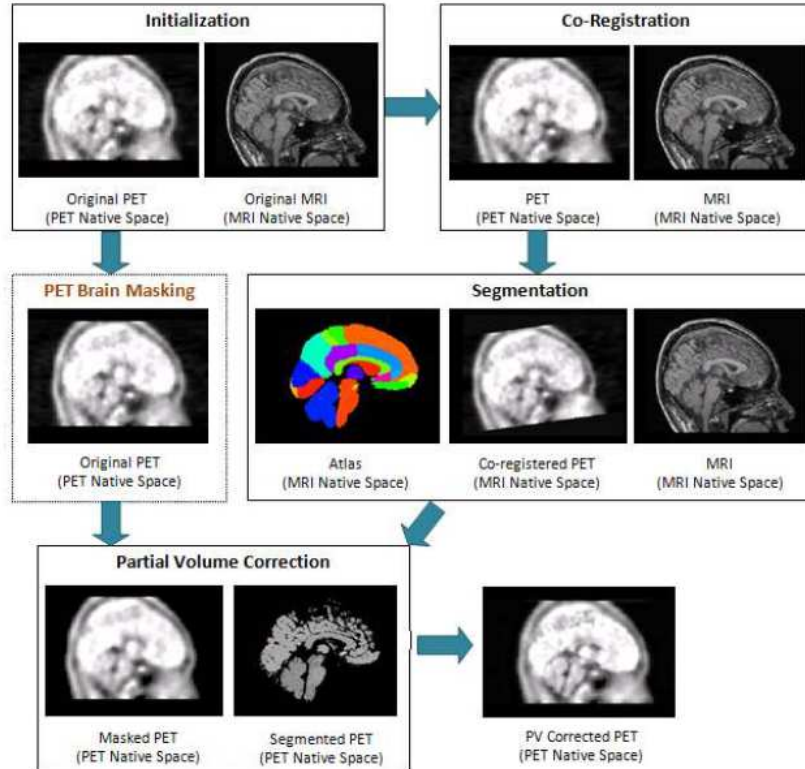


Figure 3.1: Overview of SFSRR steps. [54]

3.2 Simulated Data

A simple experiment using simulated data was performed in order to understand how the SFSRR procedure works.

3.2.1 Data creation

Simulated data was created in MATLAB in a total of four datasets:

- *True data*;
- *PET data*;
- *Segmented PET data*;
- *Smoothed Segmented PET data*.

It was chosen that simulated data would have 200x200x8 as dimensions and 0.25x0.25x1 mm³ as voxel size which corresponds to phantom data features.

3.2.1.1 True data

True data aims to recreate the original features of a square object without the blurring caused by PET low spatial resolution. For this purpose, *True data* was generated so that in the centre there was a square which voxels had the same intensity 1000 while outside were 0. This premise was considered in all eight slices (Figure 3.2).

3.2.1.2 PET data

PET data was produced by applying a 2D Gaussian filter (FWHM=2mm) to *True data*. This FWHM value was used to guarantee the existence of at least 20% of PVEs, more specifically *True data* has 1000 as maximum and PET data should not have more than 800 as maximum.

$$\text{PET image} = \text{True image} \otimes \text{Gaussian filter} \quad (3.1)$$

All data slices were created according to this methodology. The resulting data is shown in Figure 3.2.

3.2.1.3 Segmented PET data

Segmented PET data was originated by changing square's voxels values by the regional PET mean value (Figure 3.2). The mean value obtained was 503.3.

3.2.1.4 Smoothed Segmented PET data

Finally, *Smoothed Segmented PET data* was created by convolving *Segmented PET data* with a 1.5mm 2D Gaussian filter.

$$\text{Smoothed Segmented PET data} = \text{Segmented PET data} \otimes \text{Gaussian filter} \quad (3.2)$$

Smoothed Segmented PET data is shown in Figure 3.2.

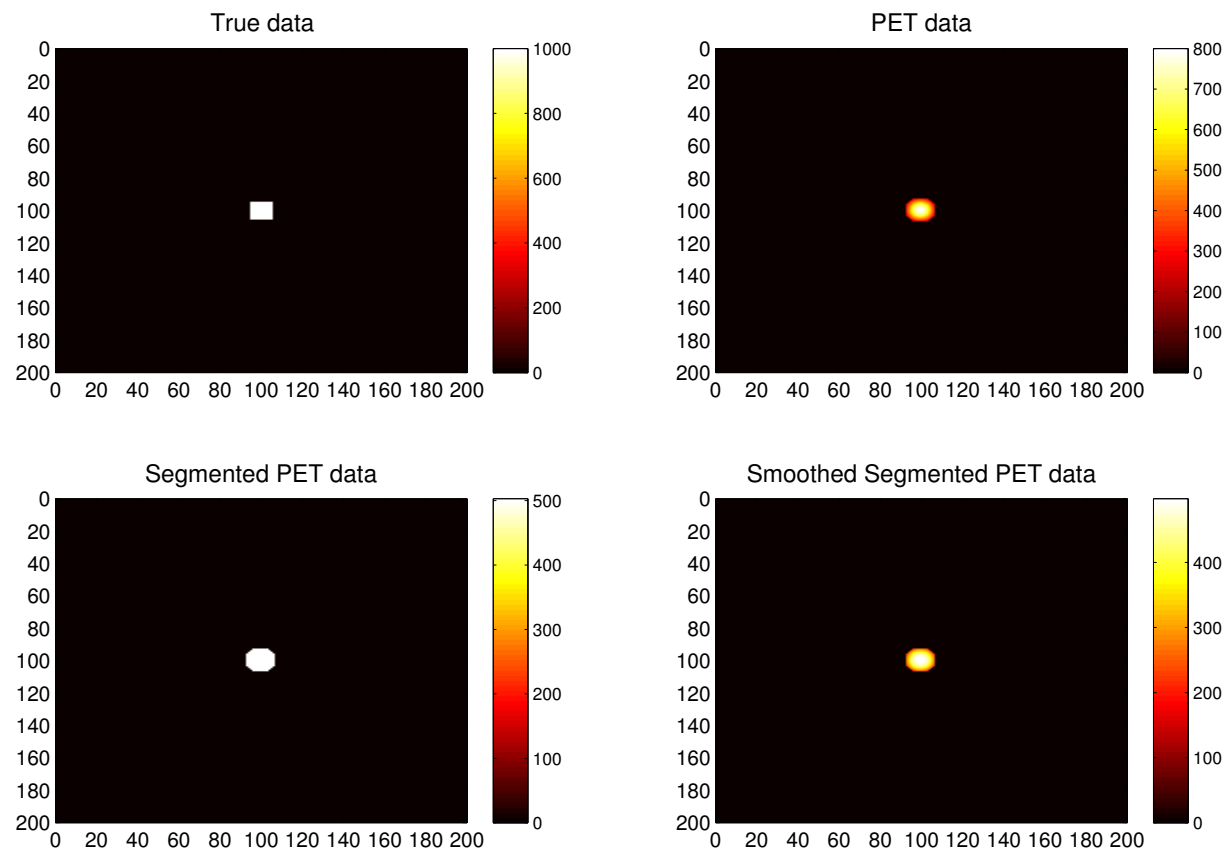


Figure 3.2: Top to bottom, from left to right: True, PET, Segmented PET and Smoothed Segmented PET datasets.

3.2.1.5 Convert data into int16 datatype and Analyze format

SFSRR method has the following requirements in terms of:

- Datatype
 - Int16 $[-32768, 32767]$;
 - Int 32 $[-2147483648, 2147483647]$;
 - Double $[-10^{308}, 10^{308}]$.
- Format
 - Analyze;
 - Nifti.

In this context, all datasets were converted into int16 and then imported from MATLAB [48] into Fiji software [63], through Miji plugin [61], so that they could be saved in Analyze format.

3.2.2 Partial Volume Correction using SFSRR procedure

PVC of simulated data was performed by using SFSRR procedure. In this case, as the data was already processed, *i.e.* the usual steps – *Initialization*, *Co-registration*, *PET Brain Masking* and *Segmentation* - were not required and so just the SFSRR_mod script was used.

This script is responsible for applying the SFSRR procedure into PET data and it uses three input files:

- *PET data*;
- *Segmented PET data*;
- *Smoothed Segmented PET data*.

Input data	Intensity Range [Bq/ml]
PET	[0,800]
Segmented PET	[0,503]
Smoothed Segmented PET	[0,498]

Table 3.1: Intensity range for different SFSRR input data: PET, Segment PET and Smoothed PET.

The output file is a new PET dataset - *Corrected PET data* (Table 3.2).

Recovered data	Intensity Range [Bq/ml]
Corrected data	[-146,976]

Table 3.2: Intensity range for Corrected data.

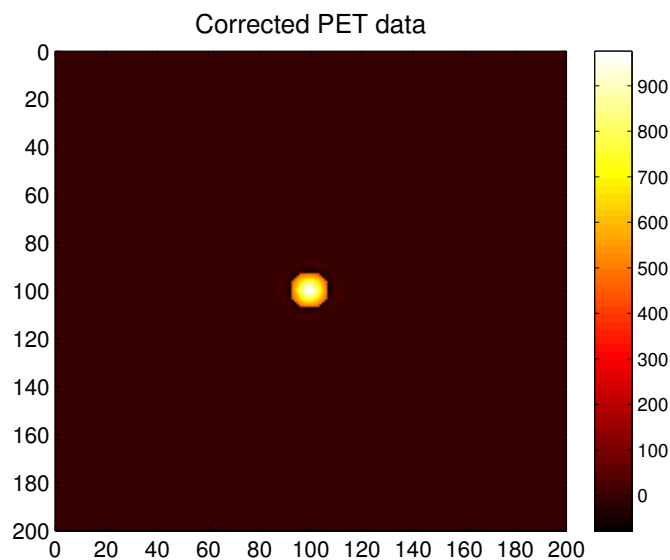


Figure 3.3: Corrected PET data.

3.3 Phantom Data

3.3.1 Mediso nanoScan PET/MRI scanner

The phantom data used in this project was obtained through a partnership between King's College London and Karolinska Institutet.

The images were acquired in a combined Mediso nanoScan PET-MRI imaging scanner in Karolinska Institutet (Figure 3.4).



Figure 3.4: Mediso nanoScan PET/MRI scanner [74].

The MRI system accommodates an 1 Tesla permanent magnet, a gradient coil and a radiofrequency (RF) shielding that protects PET electronics components from the main magnetic field and gradients. MRI images can achieve a spatial resolution of 100 μm (microns).

On the other hand, the PET module consists of an array of LSO scintillation detectors and can originate data up to 700 μm of spatial resolution.

3.3.2 Data

The main goals for using phantom data were:

1. determine how the object size influences PVC;
2. performance of the SFSRR procedure when applying it to phantom data containing different nanoparticles and ^{18}F solutions;
3. how the smoothing affects the resolution recovery performed.

For this purpose, a *Cucumis sativus* was used as phantom due to its high water content and so it is quite distinguishable in MRI. Inside, it had twelve tubes with different diameters in order to explore the effect of the object size in PVC. Three different cylindrical tubes were used:

- Small tube (0.5 mm in diameter);
- Medium tube (1 mm in diameter);
- Big tube (1.5 mm in diameter);

All tubes were filled with solutions containing distinct concentrations of SPIO nanoparticles associated to Fluorine-18, except two tubes that had water to be used as reference (Figure 3.5). Therefore, it was possible to study the effect of nanoparticles and ^{18}F concentrations in the recovery performed.

Solution	Constituents	Nanoparticles Concentration [mgFe/mL]	^{18}F Activity [Bq/ml]
A	SPIOs and ^{18}F	0.02500	4.32×10^7
B	SPIOs and ^{18}F	0.01250	2.16×10^7
C	SPIOs and ^{18}F	0.00625	1.08×10^7
Water	Water	0.00000	0.00×10^7

Table 3.3: Nanoparticles and tracer concentrations evaluated in phantom data.

The influence of smoothing in the SFSRR procedure was analysed by considering different *Smoothed Segmented PET* datasets as one of the input files of this PVC approach. This aspect is described in more detail in Section 3.3.5.

Data was acquired by performing a simultaneous 63 min PET-MRI scan.

T_2 -weighted MRI images were acquired to explore the T_2 contrast ability of SPIO nanoparticles, enabling to determine the exact location of the tubes in *Cucumis sativus*.

In terms of PET data, a static dataset was acquired and reconstructed using 3D adjMC method which employs an iterative maximum likelihood estimation method (ML-EM/OSEM) associated to an Adjoint Monte Carlo approximation (adjMC) [43].

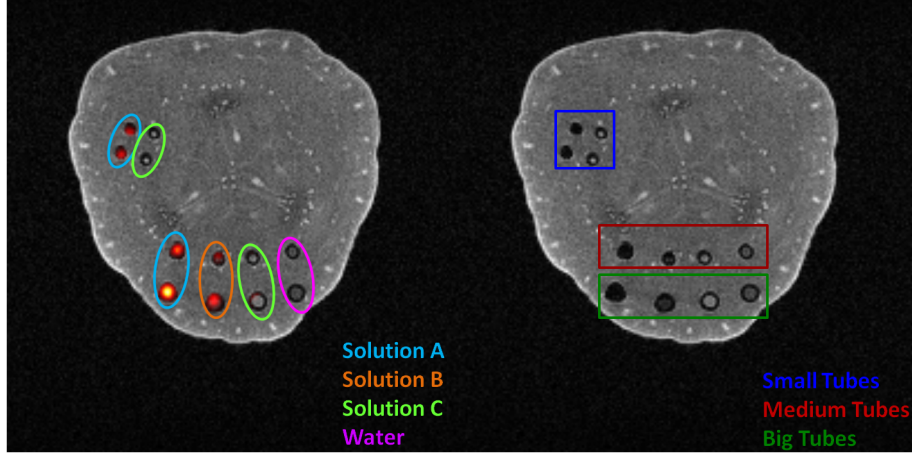


Figure 3.5: Solutions and corresponding tubes present in *Cucumis sativus*.

Parameters	Description
Iterations	20
Subset	1
Energy Window	400-600 keV

Table 3.4: Parameters used in PET data reconstruction.

3.3.3 Experiments for defining an Image Processing protocol

3.3.3.1 Original phantom data features

The image processing protocol that comes with the SFSRR procedure is just applicable to PET brain images. Therefore, an image processing protocol suitable for phantom data had to be developed.

For this purpose, the requirements of the SFSRR methodology were considered:

- Images - 3D static PET images and CT/MRI anatomical images can be used;
- Datatype
 - Int16 $[-32768, 32767]$;
 - Int 32 $[-2147483648, 2147483647]$;
 - Double $[-10^{308}, 10^{308}]$.

- Format
 - Analyze;
 - Nifti.

The features of PET and MRI original datasets are shown in Tables 3.5 and 3.6.

Modality	Description	
MRI	Dimensions	200x200x8
	Voxel size	0.25x0.25x1 (mm ³)
	Intensity range	[0,145997]
	Datatype	Unsigned short 16 (uint16)
	Scaling factor	$S_M = 35.652500$
	File format	DICOM

Table 3.5: MRI data features.

Modality	Description	
PET	Dimensions	200x200x200
	Voxel size	0.25x0.25x0.25 (mm ³)
	Intensity range	[0,4.12x10 ⁷] (Units: Bq/ml)
	Datatype	Unsigned short 16 (uint16)
	Scaling factor	$S_P = 628.206604$
	File format	DICOM

Table 3.6: PET data features.

PET and MRI data are represented according to unsigned short 16 bits (uint16) datatype which intensity range is [0,65535], however in both cases their maximum intensity goes beyond the uint16 maximum value:

- MRI - [0, 145997];
- PET - [0, 4.12 × 10⁷].

This occurs because a scaling factor multiplying with the different intensity values was used:

$$S * [a, b] \quad (3.3)$$

where S is the scaling factor, a and b are the minimum and maximum values, respectively.

Modality	No scaling factor	Considering scaling factor
PET	$[0, 2^{16}] \leftrightarrow [0, 65536]$	$628.206604 * [0, 65536] \leftrightarrow [0, 4.12 \times 10^7]$
MRI	$[0, 2^{12}] \leftrightarrow [0, 4096]$	$35.652500 * [0, 4096] \leftrightarrow [0, 145997]$

Table 3.7: Intensity range of PET and MRI in absence or not of a scaling factor.

3.3.3.2 SPM

The first software evaluated for defining an image processing protocol was SPM (Statistical Parametric Mapping) [22].

In SPM, phantom data processing was done according to the following steps:

1. Convert data from DICOM to Analyze format;
2. Data reorientation;
3. Coregistration.

Most scanners save data in DICOM format, where there is one file per slice (and per timepoint in case of dynamic data). So, firstly PET and MRI data were converted into Analyze format.

Then, as MRI and PET datasets had different orientations (Figure 3.6), PET data was flipped 180 degrees according the y-axis. The resulting data is shown in Figure 3.7.

In spite of flipping PET data, MRI and PET datasets were still not perfectly overlaid (Figure 3.7), so translations in PET data needed to be done. However, PET and MRI data had distinct dimensions and voxel size and so they could not be loaded at the same time, so translations done in phantom data could lead to errors. Therefore, another software called AMIDE was evaluated for processing the data.

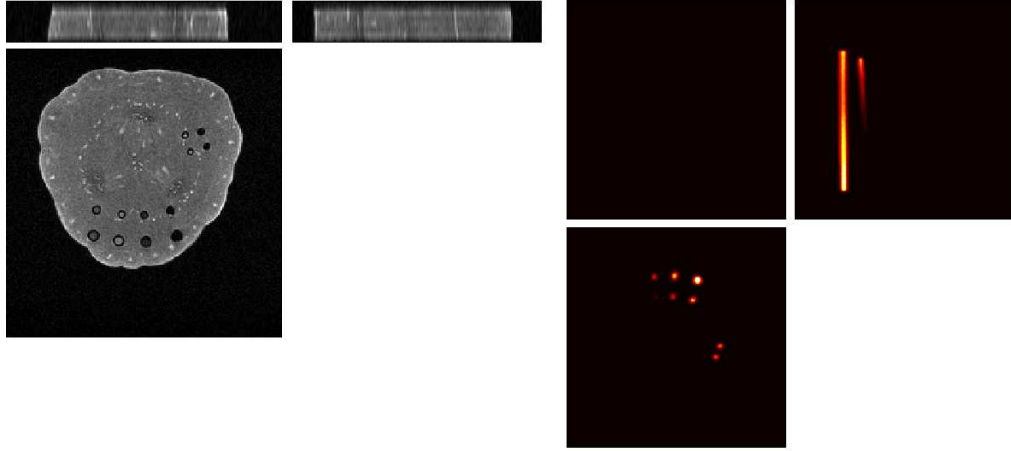


Figure 3.6: Left: Original MRI data in SPM. Right: Original PET data in SPM.

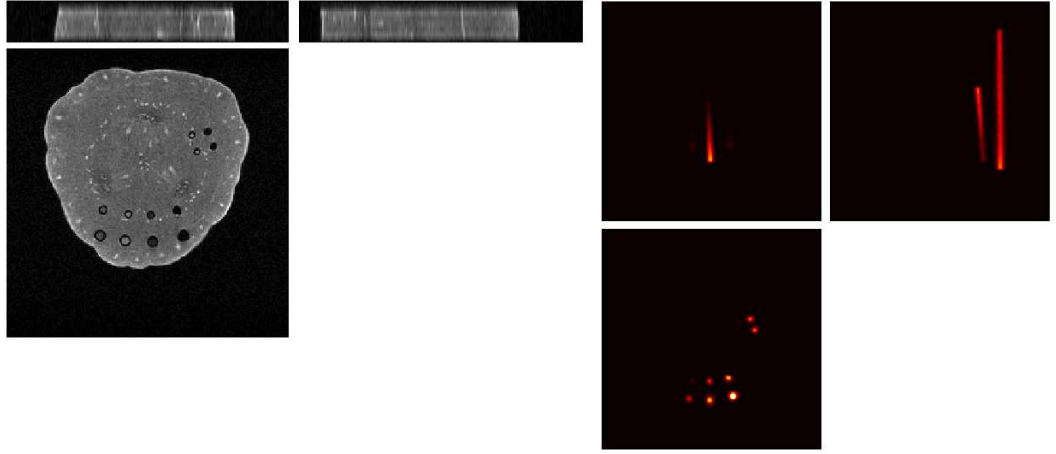


Figure 3.7: Left: Original MRI data in SPM. Right: Flipped PET data in SPM.

3.3.3.3 AMIDE

AMIDE is a free software for analyzing and registering medical imaging datasets [39].

First of all, PET and MRI images were loaded into AMIDE (Figure 3.8).

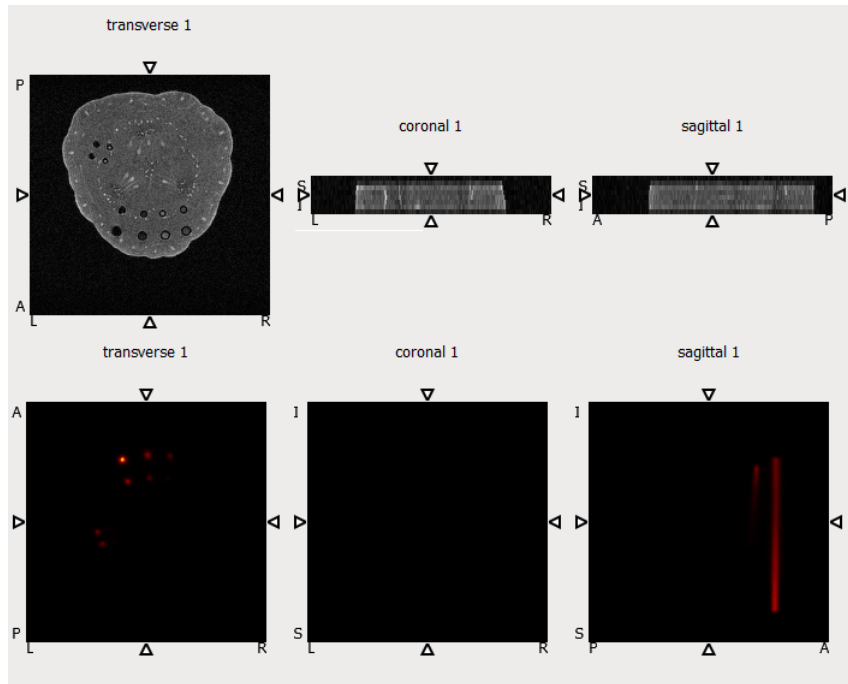


Figure 3.8: Images load into AMIDE software. Top: MRI original data; Bottom: PET original data.

Both datasets are not perfectly overlaid, so manual corrections were per-

formed:

- Change data centers;
- Reorientation;
- Translations.

PET and MRI data centers were changed to: (i) $x=0$ mm; (ii) $y=0$ mm and (iii) $z=0$ mm.

Modality	Initial data center	New data center
MRI	x: -225.00 mm y: 275.00 mm z: -0.50 mm	x: 0.00 mm y: 0.00 mm z: 0.00 mm

Table 3.8: MRI data centers.

Modality	Initial data center	New data center
PET	x: -1.88 mm y: -5.13 mm z: -119.18 mm	x: 0.00 mm y: 0.00 mm z: 0.00 mm

Table 3.9: PET data centers.

The following step consisted in flipping PET data 180 degrees according the y-axis so that it has the same orientation as MRI data.

Then, PET data was submitted to two translations:

- x: -2.0 mm;
- y: 5.6 mm.

Figure 3.9 shows PET and MRI data after performing these changes.

The last step consisted in registering data. PET and MRI data have distinct dimensions and voxel size: MRI dimensions are $200 \times 200 \times 8$ and voxel size is $0.25 \times 0.25 \times 1$ mm³, while in PET are respectively $200 \times 200 \times 8$ and $0.25 \times 0.25 \times 0.25$ mm³. For these conditions, AMIDE automatically registered PET data to a voxel size of $0.25 \times 0.25 \times 1$ mm³ and $208 \times 223 \times 50$ as dimensions. However, since we would like PET data to have the same dimensions as MRI data, we decided to use another software for processing phantom data.

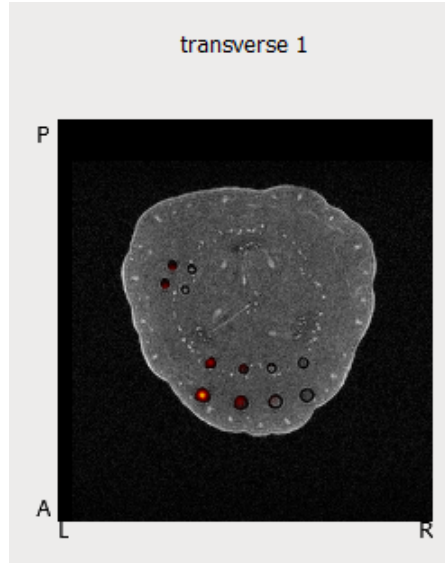


Figure 3.9: MRI and PET data after transformations.

3.3.4 Final Image Processing protocol

After the previous trials, it was chosen that MRI and PET data would be processed by using the following softwares:

- VivoQuant [28];
- Fiji [63];
- MATLAB [48].

The processing approach selected will be explained in more detail in the following subsections.

3.3.4.1 VivoQuant

VivoQuant is inviCRO's multi-modality post-processing software which can be used for SPECT, CT, PET, MR and optical imaging data [28].

This software was selected for reorienting the data and performing image registration, because data reslice and resample in VivoQuant are performed automatically without requiring user intervention.

First of all, PET and MRI original data were imported into VivoQuant. The intensity range of PET data changed because VivoQuant automatically modifies the voxel size and dimensions of PET data so that it matches the features of the reference image, in this case the MRI dataset, which are 200x200x8 as dimensions and 0.25x0.25x1 mm³ as voxel size. The new intensity values of PET and MRI data are shown in Tables 3.10 and 3.11.

PET original data	New PET data
$[0, 4.12 \times 10^7]$	$[0, 3.58 \times 10^7]$

Table 3.10: PET intensity values.

MRI original data	New MRI data
$[0, 145997]$	$[0.005, 145997]$

Table 3.11: MRI intensity values.

MRI and PET images have different orientations (Figure 3.10).

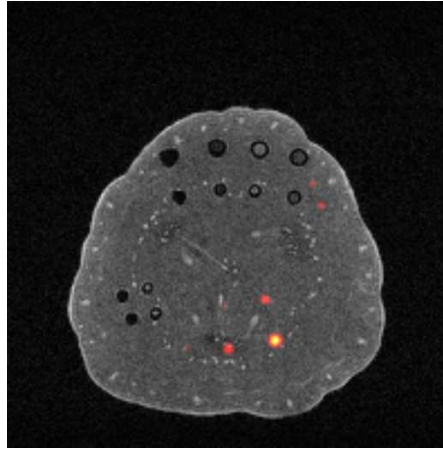


Figure 3.10: Initial orientation of PET and MRI data.

MRI data was reoriented 180 degrees in the x-axis direction. On the other hand, PET images were flipped 180 degrees in the y-axis direction.

Even after flipping, PET and MRI images were not perfectly overlaid (Figure 3.11).

So, PET data was manually corrected by using the following translation values:

- Translation x-axis: -2.0 mm;
- Translation y-axis: -5.6 mm.

The result obtained is displayed in Figure 3.12.

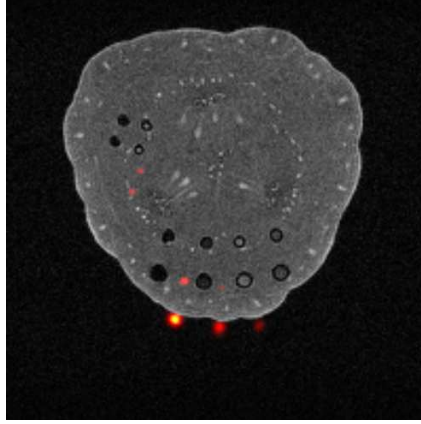


Figure 3.11: MRI and PET dat after flipping.

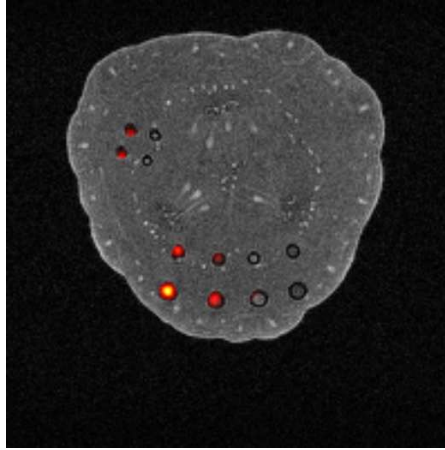


Figure 3.12: MRI and PET data after translation.

It is important that after the processing steps, MRI and PET have the same format and datatype.

Related with the data format, it was chosen to export the images in Raw format because when saving as DICOM format in VivoQuant this software locks certain features of the images, which then are not detectable by other imaging softwares.

In terms of datatype, single-precision 32-bit floating-point representation, float32 $[10^{-38}, 10^{38}]$ was considered for describing more accurately the intensity values of the data without requiring the use of scaling factors as it happened in the original data (Table 3.7).

Table 3.12 shows the new features of MRI and PET datasets.

Modality	Description	
MRI	Intensity Range	[0,145997]
	Datatype	Float32
	File format	Raw
PET	Intensity Range	[0,3.58x10 ⁷]
	Datatype	Float32
	File format	Raw

Table 3.12: MRI and PET new data features.

3.3.4.2 Fiji

Fiji is a distribution of ImageJ that allows performing image processing and data analysis [63].

MRI data in Raw format was opened in Fiji and ROIs corresponding to the location of the different tubes were drawn. The same strategy was applied to all eight slices and therefore eight ROI maps were created.

3.3.4.3 MATLAB

MATLAB is a programming language and software which can be applied to analyse data, create algorithms and models, as well as to develop other applications [48].

PET Masking

In PET data is not possible to distinguish the exact location of all tubes. Consequently, ROI maps generated with Fiji were imported into MATLAB by using MIJ plugin which allows exchange data between these two softwares.

These maps were used to mask *Registered PET data*, originating *Masked PET data* (Figure 3.13).

ROIs and Mean

The aim of ROIs and Mean step was to assess each tube ROI and then change their voxels values by the regional PET mean value, resulting in *Segmented PET data* (Figure 3.13).

Smoothing

The final dataset created was *Smoothed Segmented PET data* which is originated by convolving *Segmented PET data* with a 2D Gaussian filter.

$$\text{Smoothed Segmented PET data} = \text{Segmented PET data} \otimes \text{Gaussian filter} \quad (3.4)$$

Different values of FWHM were used in order to evaluate how the smoothing affects the efficiency of the SFSRR procedure. As real data has 200x200x8 as dimensions and 0.25x0.25x1 mm³ of voxel size, the FWHM values chosen were:

- 0.8 mm;
- 1 mm;
- 1.2 mm;
- 1.4 mm.

In total, four *Smoothed Segmented PET datasets* were created which have the following denominations (Figure 3.13):

- *S1 - Smoothed Segmented PET dataset* obtained when using a Gaussian filter with FWHM=0.8mm;
- *S2 - Smoothed Segmented PET dataset* originated by applying a Gaussian filter with FWHM=1mm;;
- *S3 - Smoothed Segmented PET dataset* created with a Gaussian filter that has FWHM=1.2mm;
- *S4 - Smoothed Segmented PET dataset* generated when using a Gaussian filter that has FWHM=1.4mm.

Export data

In SFSRR procedure, data must obey to the following requirements:

- Datatype
 - int16 which range of values is $[-32768, 32767]$;
 - in32 with $[-2147483648, 2147483647]$;
 - double that has the following values interval $[-10^{308}, 10^{308}]$.
- Format
 - Analyze;
 - Nifti.

Thus, *Masked PET*, *Segmented PET* and *Smoothed Segmented PET datasets* were exported from MATLAB in Analyze format and double datatype to comply with SFSRR requirements.

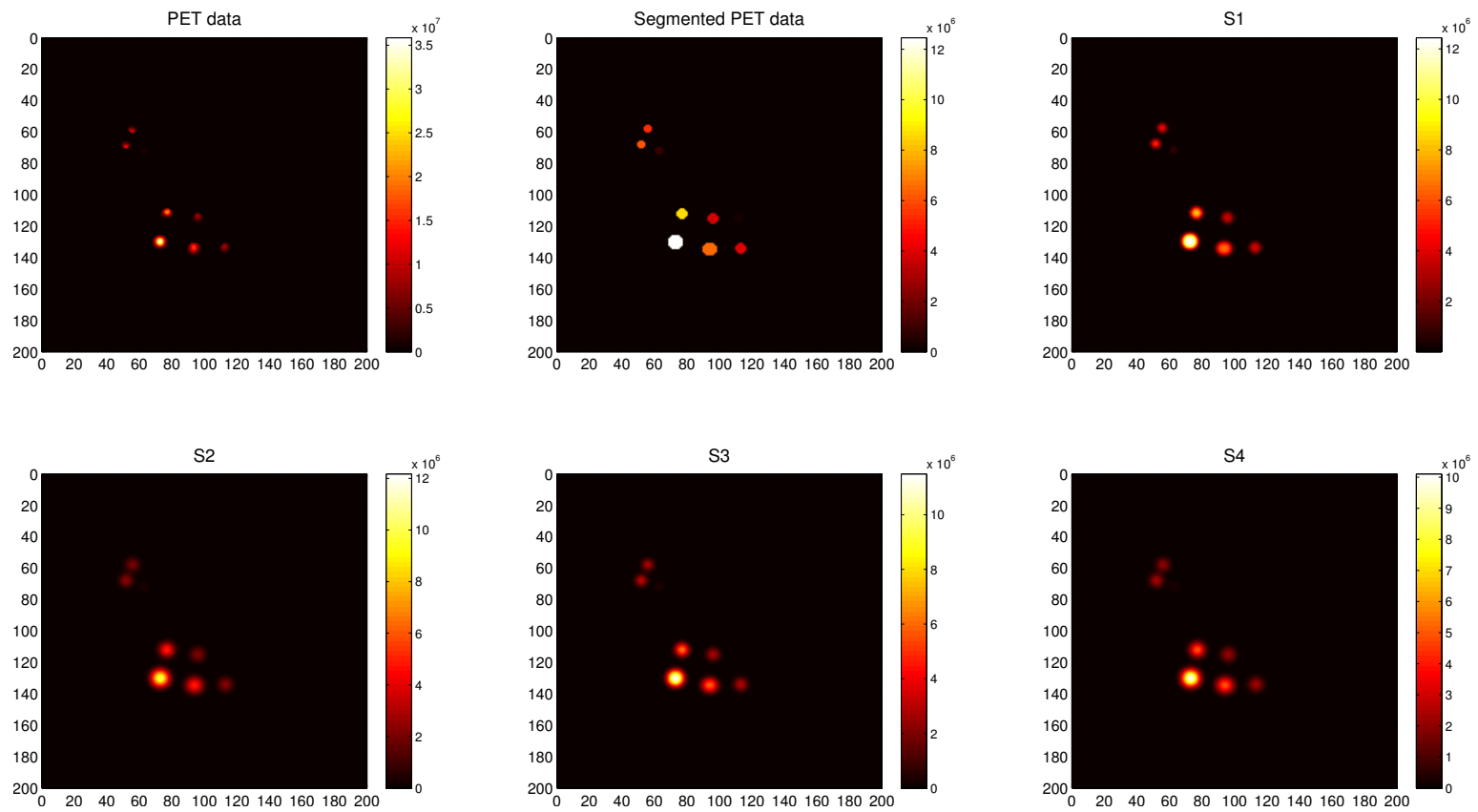


Figure 3.13: Top to bottom, from left to right: True, PET, Segmented PET and Smoothed Segmented PET datasets.

3.3.5 Partial Volume Correction using SFSRR procedure

Partial volume correction of the real data was performed by using the SFSRR procedure, more specifically the SFSRR_mod script, as the data was already processed, and so it was not required to do the usual steps – *Initialization*, *Co-registration*, *PET Brain Masking* and *Segmentation*.

Three input files were used (Table 3.13):

- *PET data*;
- *Segmented PET data*;
- *Smoothed Segmented PET data*.

As in total four *Smoothed Segmented PET datasets* - *S1*, *S2*, *S3* and *S4* - were created in order to assess the efficiency of the SFSRR, the procedure was applied four times.

Input data	Intensity range [Bq/ml]
PET	$[0,3.58 \times 10^7]$
Segmented PET	$[0,1.39 \times 10^7]$
S1	$[0,1.38 \times 10^7]$
S2	$[0,1.32 \times 10^7]$
S3	$[0,1.16 \times 10^7]$
S4	$[0,1.01 \times 10^7]$

Table 3.13: Input data and Corrected PET datasets 1 to 4, which correspond to the recovery data when using, respectively, *S1* to *S6* as *Smoothed Segmented PET data*.

The output file of the SFRSS approach is a new PET image (*Corrected PET data*).

Table 3.14 shows the intensity ranges of *Corrected PET datasets*.

Recovered data	Intensity range [Bq/ml]
Corrected PET data 1	$[-1.13 \times 10^7, 5.53 \times 10^7]$
Corrected PET data 2	$[-1.53 \times 10^7, 6.31 \times 10^7]$
Corrected PET data 3	$[-1.88 \times 10^7, 6.99 \times 10^7]$
Corrected PET data 4	$[-2.28 \times 10^7, 7.74 \times 10^7]$

Table 3.14: Corrected PET datasets 1 to 4, which correspond to the recovery data when using, respectively, *S1* to *S4* as *Smoothed Segmented PET data*.

Chapter 4

Results and Discussion

4.1 Simulated data

4.1.1 Intensity Range

True, simulated, segmented, smoothed and recovered images are shown in Figure 4.1. There are differences between *PET data* and *Corrected PET data* upon visual inspection. This becomes more clear when observing Table 4.1, as the minimum value changed from 0 to -146 and the maximum value changed from 800 to 976.

Simulated data	Intensity Range [Bq/ml]
True data	[0,1000]
PET data	[0,800]
Segmented PET data	[0,503]
Smoothed Segmented PET data	[0,498]
Corrected PET data	[-146,976]

Table 4.1: Intensity ranges of simulated data.

In order to assess the location of the negative values, two regions - background and object - were defined in *PET* and Corrected PET data and the corresponding minimum, maximum and mean values were estimated (Table 4.2).

Dataset	Region	Slices	Min [Bq/ml]	Max [Bq/ml]	Mean \pm S.D. [Bq/ml]
PET data	Object	1 to 8	277.0	800.0	503.3 \pm 155.7
	Background		0.0	0.0	0.0 \pm 0.0
Corrected data	Object	1 to 8	406.5	850.5	557.4 \pm 122.7
	Background		-117.8	23.4	-0.1 \pm 3.4

Table 4.2: Minimum, maximum and mean values of the regions identified in PET and Corrected data.

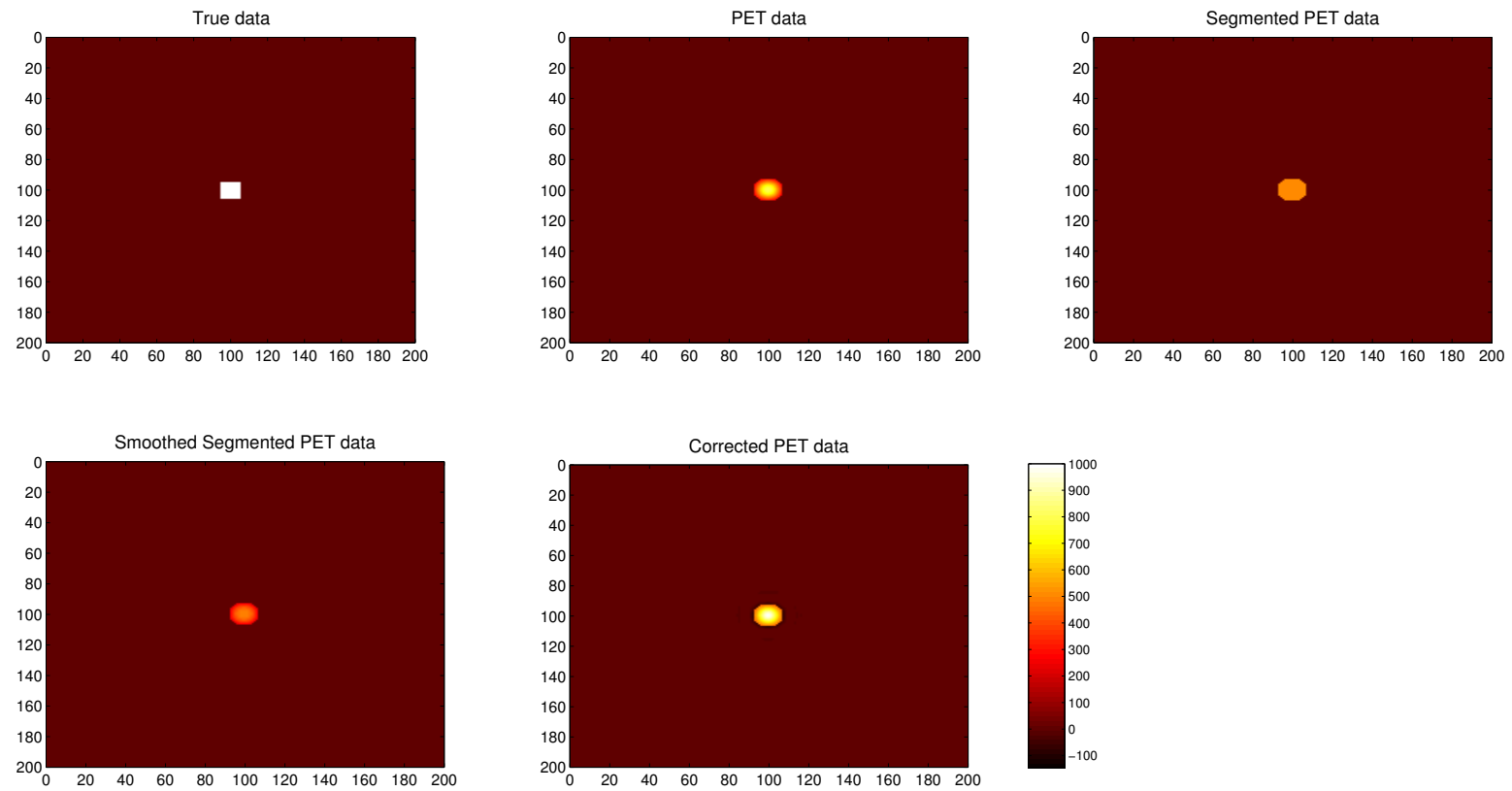


Figure 4.1: Simulated images (Top to bottom, from left to right): True data, PET data, Segmented PET data; (bottom, from left to right) Smoothed Segmented PET data and Corrected PET data obtained with SFSRR method.

The negative values detected in *Corrected PET data* are located in the background and in the boundary between this region and the object (Figure 4.2). This might be related with the difficulty of the wavelet transform in decomposing circular objects. However, this aspect does not compromise the resolution recovery performed, as the important PET counts are located inside the object and not in the surrounding areas.

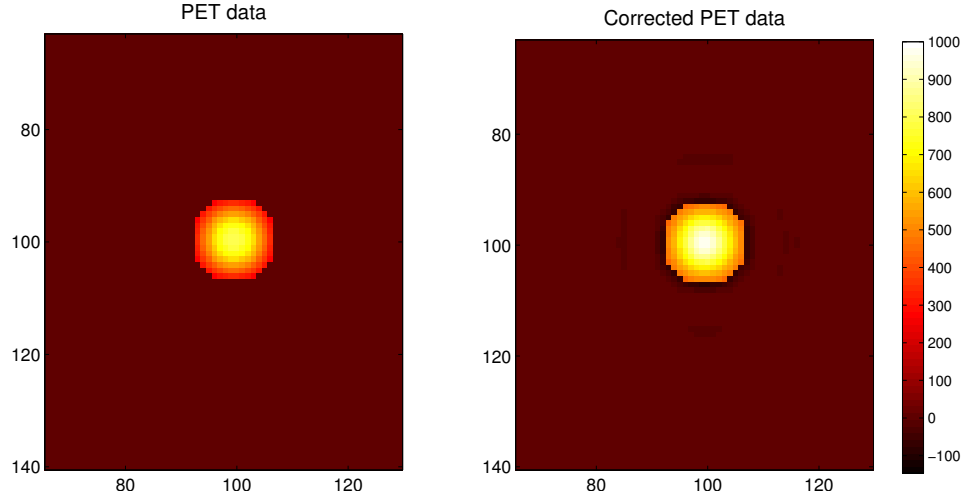


Figure 4.2: Zoomed images. Left: PET data; Right: Corrected PET data.

4.1.2 Intensity differences in the different slices

True, *PET*, *Segmented PET* and *Smoothed Segmented PET* datasets were created so that all the 8 slices would be equal, *i.e.*, would have the same intensity features, but it did not occur after performing PVC when analysing *Corrected PET data*. This aspect can be seen in more detail in Figure 4.3 which shows the transverse and coronal views of *PET* and *Corrected PET* datasets, as well as in the line profiles defined in both datasets (Figure 4.4).

The expected results would be that all slices of *Corrected PET data* had the same intensity values considering the initial conditions of input data - *PET*, *Segmented PET* and *Smoothed Segmented PET* datasets - however this did not happen. Therefore, further studies in this regard are necessary.

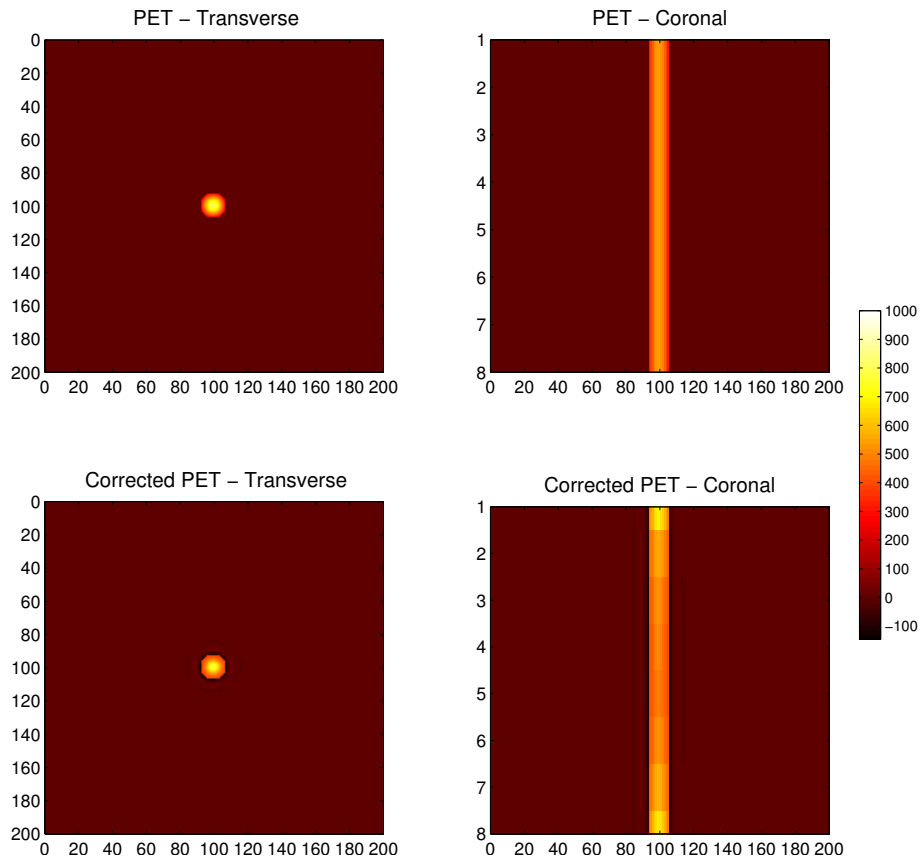


Figure 4.3: Transverse and Coronal views of PET and Corrected PET datasets.

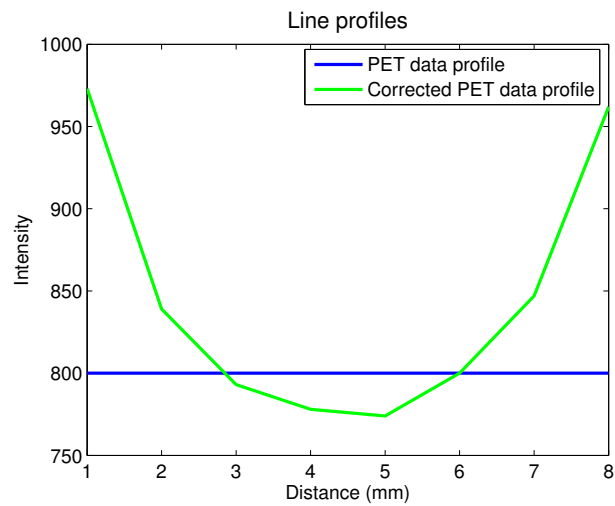


Figure 4.4: Line profiles from PET and Corrected PET datasets.

4.1.3 Partial Volume Correction

For checking the changes introduced by the SFSRR method, the maximum and mean values from *PET* and *Corrected PET* datasets were calculated (Tables A.1 and A.2). The *Difference* between recovered values in *Corrected PET data* and the original values in *PET data* was estimated by using the following expression:

$$Difference = \left[\left(\frac{recovered\ value}{original\ value} \right) - 1 \right] \times 100\% \quad (4.1)$$

Certain slices showed an increase in terms of the maximum values, more specifically between 0.8% and 22.0%. The maximum values in Slices 1 and 8 of *Corrected PET data*, respectively 976 and 965, did not differ significantly from the intensity of *True data* which was 1000. Thus, a better recovery was achieved in these slices, 22.0% and 20.6%. On the other hand, other slices showed a small decrease in the maximum values of around -2.0% (Figure 4.5 and Table A.1 in Appendix A).

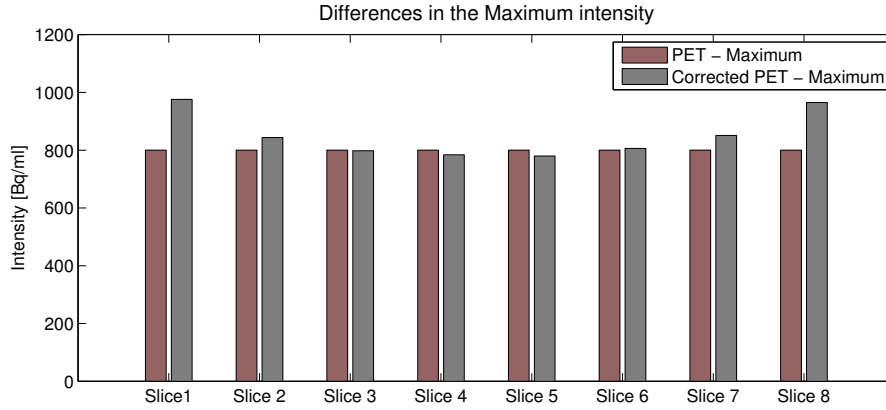


Figure 4.5: Maximum values in each slice of PET and Corrected PET datasets.

Relating to the mean values, increases were verified in the majority of the slices (Figure 4.6 and Table A.2 in Appendix A), but a slight decrease was observed in Slices 4 and 5, respectively, -0.5% and -1.2%.

As mentioned previously in Section 4.1.2, a non-uniformity in the intensities was verified in *Corrected PET data*, so the differences displayed in Figures 4.5 and 4.6 and Tables A.1 to A.2 (Appendix A) are in concordance with this aspect.

In general, the use of the SFSRR procedure translated into a global improvement of the activity, respectively, 6.8 % and 10.3% in the maximum and mean values.

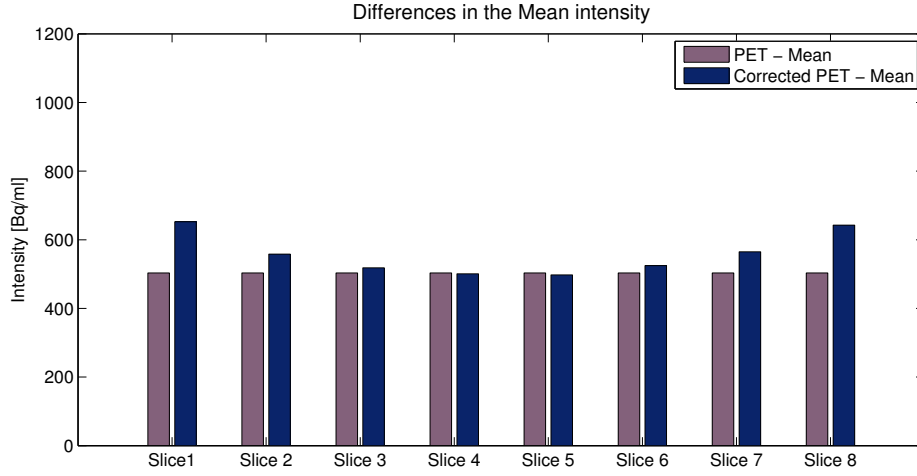


Figure 4.6: Mean values in each slice of PET and Corrected PET datasets.

4.2 Phantom data

4.2.1 Intensity Range

PET and *Corrected PET* datasets are shown in Figure 4.7 and differences are noticeable by visual inspection.

Table 4.3 displays the intensity ranges from *PET* and *Corrected PET* data.

Firstly, lower minimum values were detected in *Corrected PET data 3* and *4* where a more significant smoothing was applied to one of the input data - *Smoothed Segmented PET*. On the other hand, the maximum values increased after performing PVC.

Phantom data	Intensity Range [Bq/ml]
PET data	$[0.00 \times 10^7, 3.58 \times 10^7]$
Corrected PET data 1	$[-1.13 \times 10^7, 5.53 \times 10^7]$
Corrected PET data 2	$[-1.53 \times 10^7, 6.31 \times 10^7]$
Corrected PET data 3	$[-1.88 \times 10^7, 6.99 \times 10^7]$
Corrected PET data 4	$[-2.28 \times 10^7, 7.74 \times 10^7]$

Table 4.3: Intensity ranges of PET and Corrected data. Corrected PET datasets differ in terms of the data used as Smoothed Segmented PET data in the SFSRR procedure: (i) in Corrected PET data 1 was S1; (ii) in Corrected PET data 2 was S2; (iii) in Corrected PET data 3 was S3 and (iv) in Corrected PET data 4 was S4.

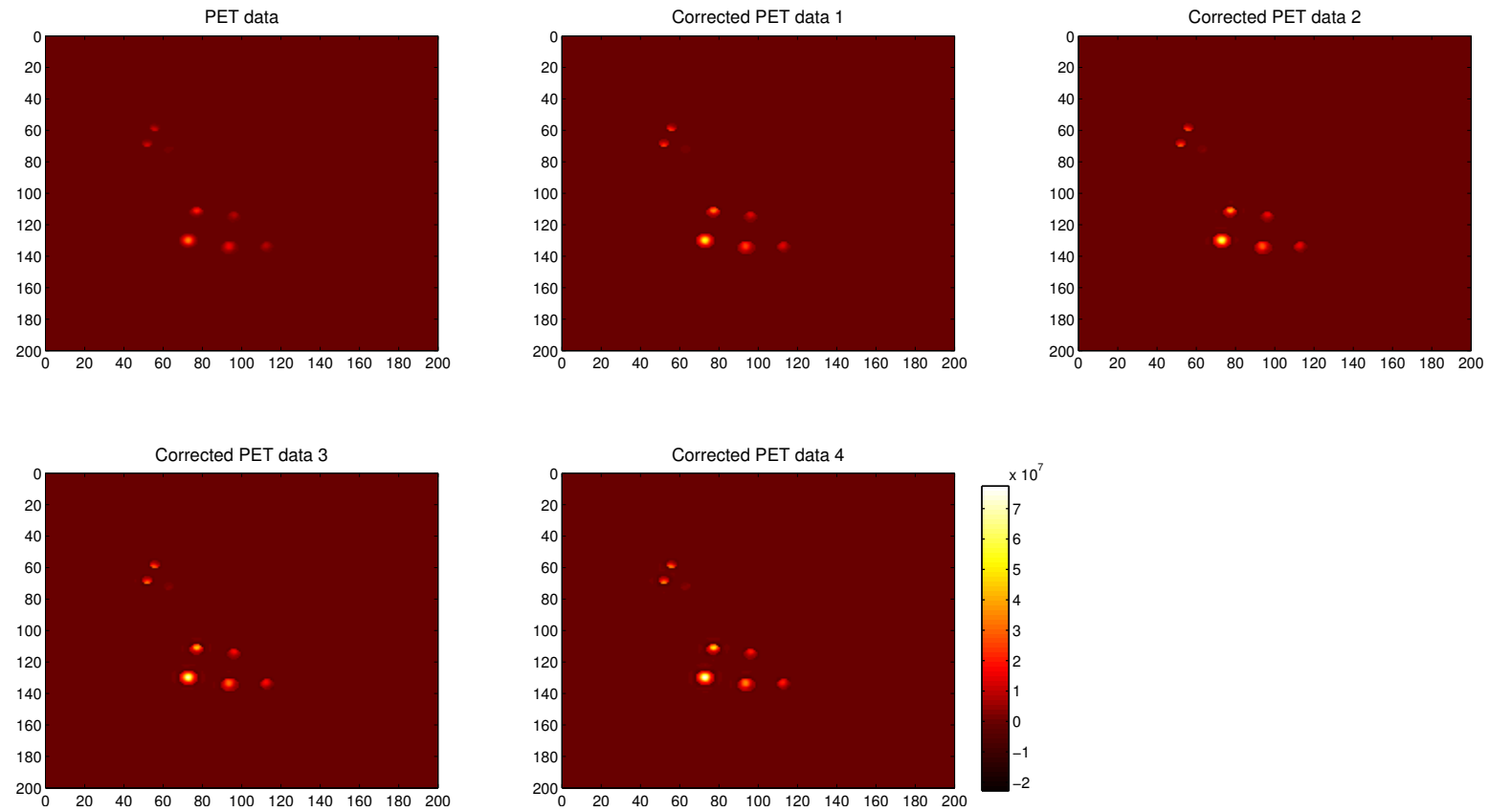


Figure 4.7: Phantom data. Top to bottom, from left to right: PET and Corrected PET data 1 to 4.

The negative values detected in *Corrected PET* are located in the boundary between the tubes and the background (Figure 4.8). This aspect was also visible in the simulated data and it might be related with the limitation of the wavelet transform at decomposing circular objects.

This situation does not compromise the resolution recovery performed as the relevant measurements are located inside the tubes and not in the boundary and background areas.

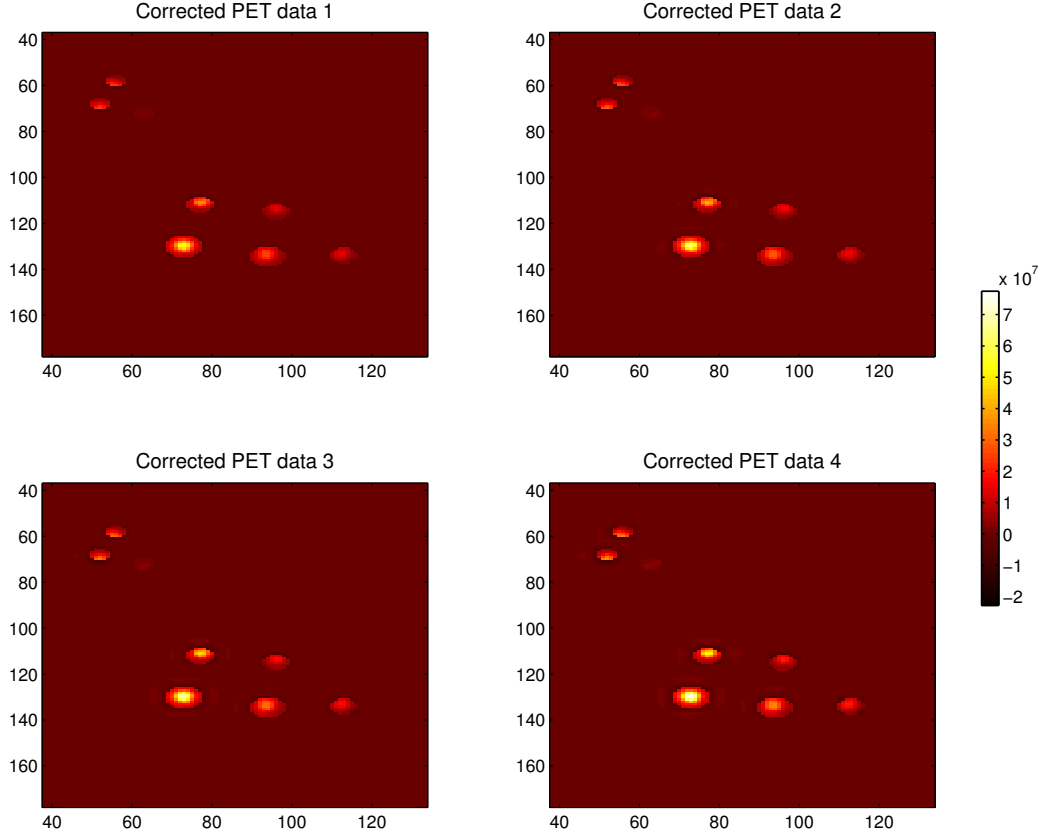


Figure 4.8: Zoomed images of Corrected PET datasets for displaying the location of the negative values.

4.2.2 Partial Volume Correction

The maximum and mean values of the tubes containing SPIOs nanoparticles and ^{18}F were estimated for *PET* and *Corrected PET* datasets. The units used were kBq/ml instead of Bq/ml in order to show more clearly the results obtained.

The changes introduced by the SFSRR procedure were assessed by estimating the *Difference* factor (Equation 4.1.3).

Figures 4.9 and 4.10 display the different tubes used in phantom data, while Table 4.4 shows the solutions evaluated.

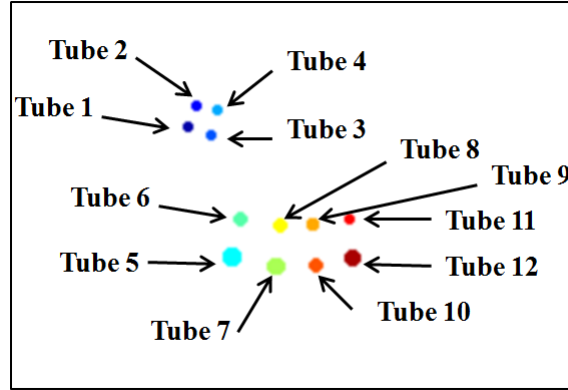


Figure 4.9: Tubes identification.

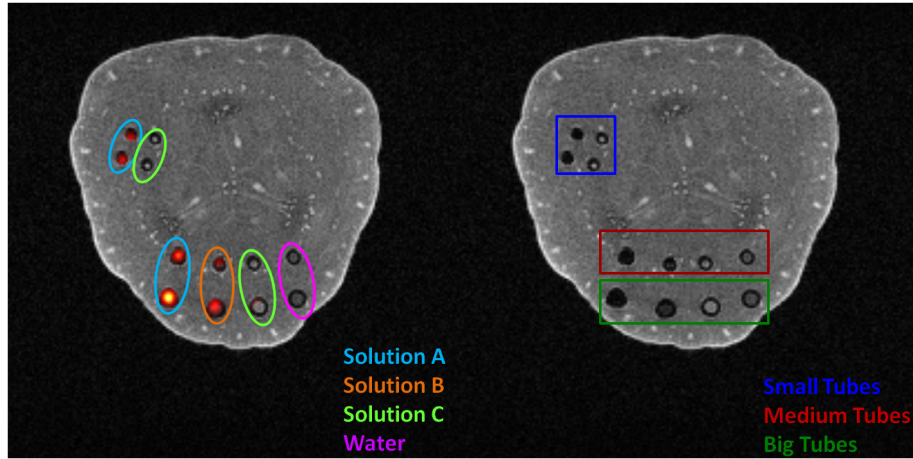


Figure 4.10: Solutions and corresponding tubes present in *Cucumis sativus*.

Solution	Constituents	Nanoparticles Concentration [mgFe/mL]	^{18}F Activity [kBq/ml]
A	SPIOs and ^{18}F	0.02500	4.32×10^4
B	SPIOs and ^{18}F	0.01250	2.16×10^4
C	SPIOs and ^{18}F	0.00625	1.08×10^4
Water	Water	0.00000	0.00×10^4

Table 4.4: Nanoparticles and tracer concentrations evaluated in phantom data.

The maximum values are shown in Figures 4.11 and Table B.1 (Appendix B).

The SFSRR procedure led to an increase in the maximum values of all tubes. Higher recovery deviations were detected in small tubes and containing a higher

concentration of nanoparticles and Fluorine-18.

Small tubes 1 and 2 with solution A, that had a higher concentration of nanoparticles and tracer, showed an average increase of 95.6 %, 128.8 %, 156.7% and 187.4% for *Corrected PET data 1 to 4*.

The second higher difference corresponded to small tubes 3 and 4 with solution C, lower content of nanoparticles and Fluorine-18, with average increases of 81.0%, 108.6%, 131.8% and 157.2% for *Corrected PET data 1 to 4*.

In medium tubes, a higher concentration of radioisotope and nanoparticles resulted in a larger recovery, around 101.0%, when comparing to solutions B and C that showed average improvements of 98.9% and 94.8%.

In contrast, higher differences in maximum values were obtained for smaller concentrations of nanoparticles and ^{18}F in big tubes. Tube 5 containing solution A had an average increase of 85.3%, while tubes 7 and 10 with solutions B and C showed a recovery of 87.4% and 101.2%.

Additionally, the mean values and the corresponding *Difference* factors were estimated in *PET* and *Corrected PET* datasets (Figure 4.12 as well as Tables B.3 and B.4 in Appendix B).

An increase in the mean values was observed in all tubes with this aspect being progressively more significant for higher smoothing values.

In order to better understand the changes in the tracer's uptake after performing PVC, the *Differences* calculated and shown in Table B.4 were organized so that three aspects could be evaluated:

- how the object size influences PVC (Section 4.2.2.1);
- performance of SFSRR procedure when applying it to phantom data with distinct concentrations of nanoparticles and Fluorine-18 (Section 4.2.2.1);
- how smoothing affects the resolution recovery performed (Section 4.2.2.2).

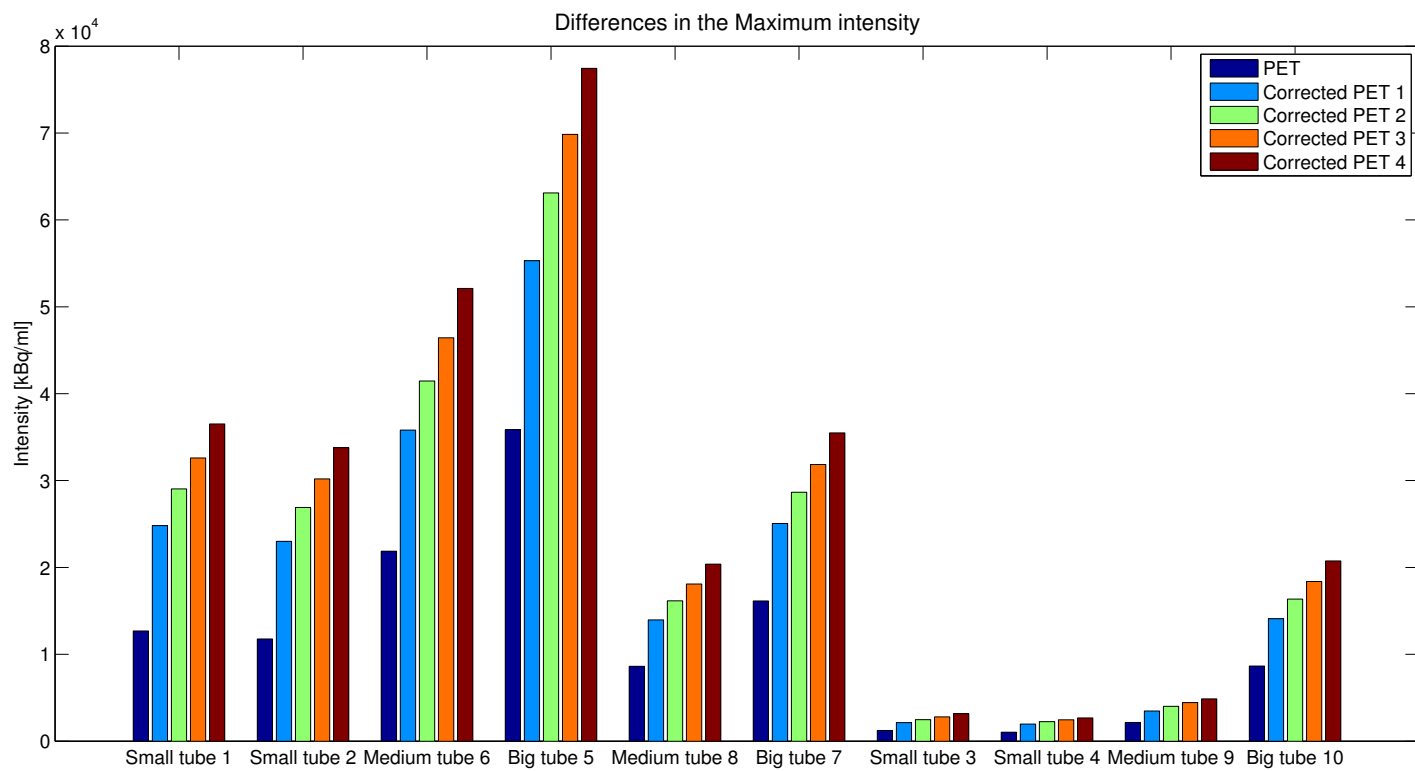


Figure 4.11: Maximum values in PET and Corrected PET datasets: Solution A - Tubes 1, 2, 6 and 5; Solution B - Tubes 8 and 7; Solution C - Tubes 3, 4, 9 and 10.

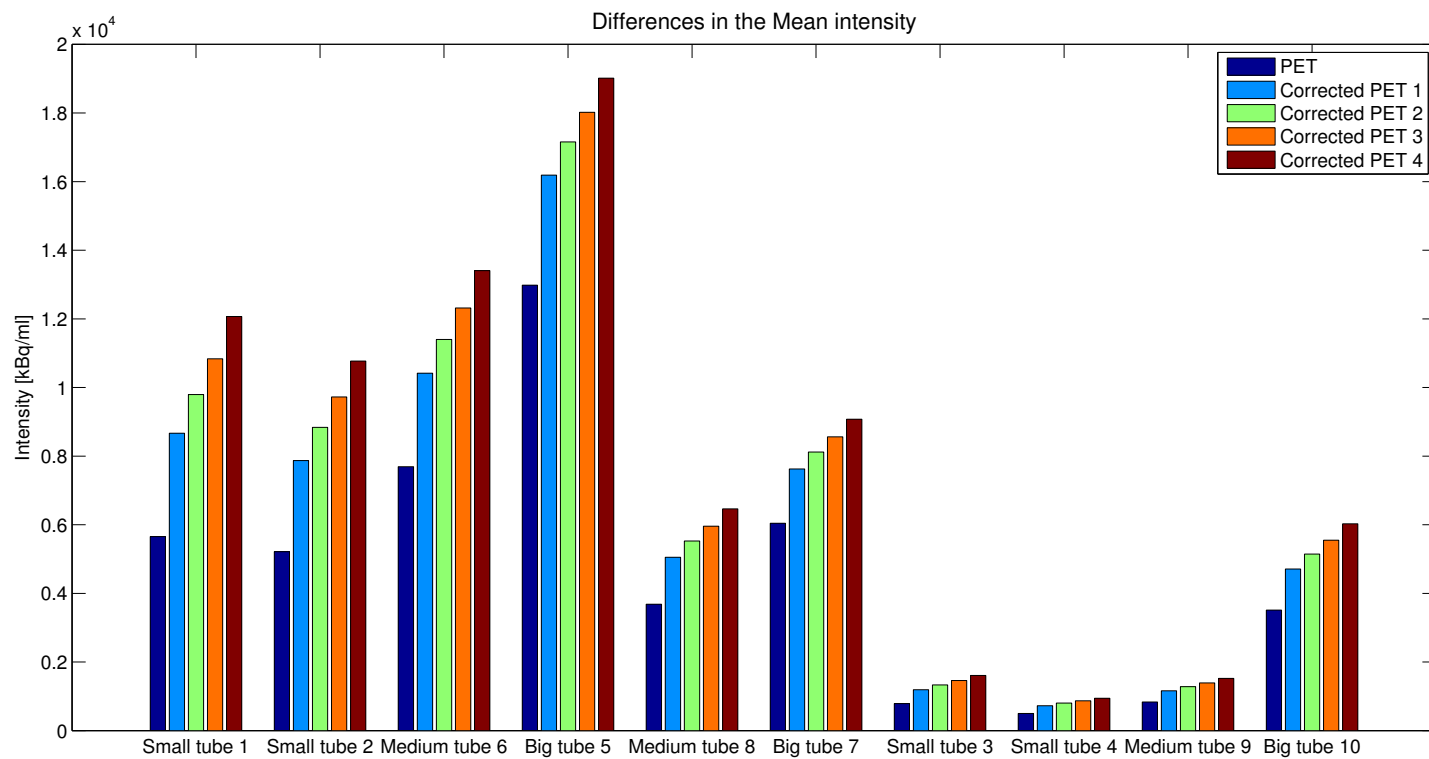


Figure 4.12: Mean values in PET and Corrected PET datasets: Solution A - Tubes 1, 2, 6 and 5; Solution B - Tubes 8 and 7; Solution C - Tubes 3, 4, 9 and 10..

4.2.2.1 Influence of the object size and nanoparticles concentrations in PVC

The influence of the object size in PVC was studied by using three different cylindrical tubes in phantom data:

- Small tube (0.5 mm in diameter);
- Medium tube (1 mm in diameter);
- Big tube (1.5 mm in diameter).

Additionally, for each tube two or more solutions were used in order to evaluate how the PVC is related with the nanoparticles and ^{18}F concentrations considered (Table 4.4).

The *Difference factors* in Table B.4 (Appendix B) were organized to show how the resolution recovery was affected by the tubes size (Figure 4.13) and nanoparticles- ^{18}F solutions (Figure 4.14).

The use of small tubes and solution A provided mean improvements within [51.0;113.5] % for the different smoothing values, while for the same object size but with a lower concentration of nanoparticles and ^{18}F (solution C) the differences observed were between 45.2 and 104.0 %.

On the other hand, greater changes in medium tubes were achieved when considering progressively a smaller concentration of nanoparticles and ^{18}F :

- Solution A - [35.4;74.3] %;
- Solution B - [37.2;75.5] %;
- Solution C - [39.5;82.6] %;

Big tubes also showed the same variation pattern than in medium tubes. Higher variations in recovery were observed when gradually a lower concentration of nanoprobe was used, however they were not so high as in medium size objects:

- Solution A - [24.7;46.5] %;
- Solution B - [26.1;50.1] %;
- Solution C - [34.2;71.7] %;

Smaller objects tend to be more affected by PVEs, resulting in a more significant blurring of the object's activity to neighbour areas and consequently greater underestimation of tracer's uptake. In this case, SFSRR originated larger variations in quantification for smaller tubes size when comparing to medium and big tubes.

In terms of the solutions evaluated, greater recovery differences in the small tubes were detected for higher concentrations of nanoparticles and ^{18}F . In contrast, PVC showed higher improvements for a lower concentration of SPIO nanoparticles and ^{18}F in medium and big tubes, however this aspect was more significant in medium tubes than in the big tubes.

4.2.2.2 Smoothing versus recovery

The *Differences* calculated (Table B.4) were used for assessing the effect of smoothing in resolution-recovery (Figure 4.15).

Higher smoothed FWHM values led to poorer spatial resolution of *Smoothed Segmented PET data* and for these conditions SFSRR originated greater improvements in all tubes.

This aspect resulted from the fixed resolution levels j considered by the method (Equation 2.12). More specifically, currently SFSRR uses fixed frequency bands for decomposing the input data which may not be ideal for the phantom data used in this project. Therefore, further experiments are required for verifying which resolution levels j are suitable for this specific data as well as to better understand how smoothing really influences the recovery performed.

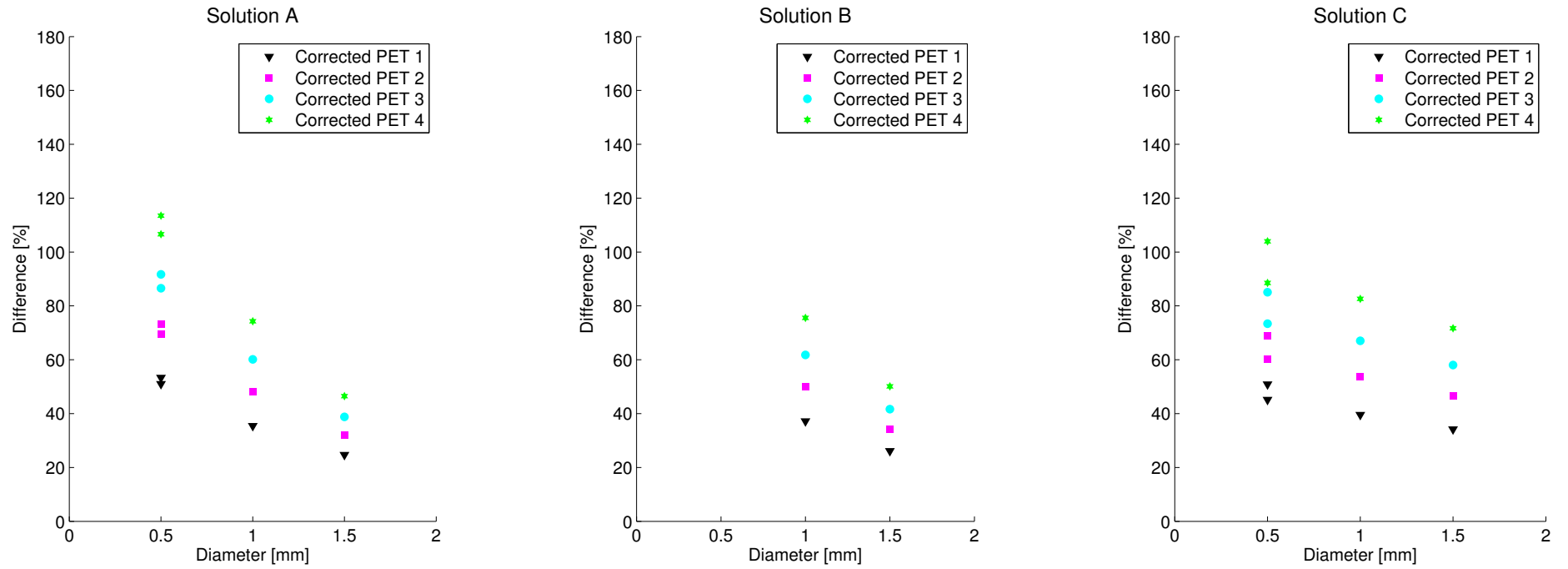


Figure 4.13: Measured *Differences* for solutions A, B, C and water depending on the tube size and the smoothing values used.

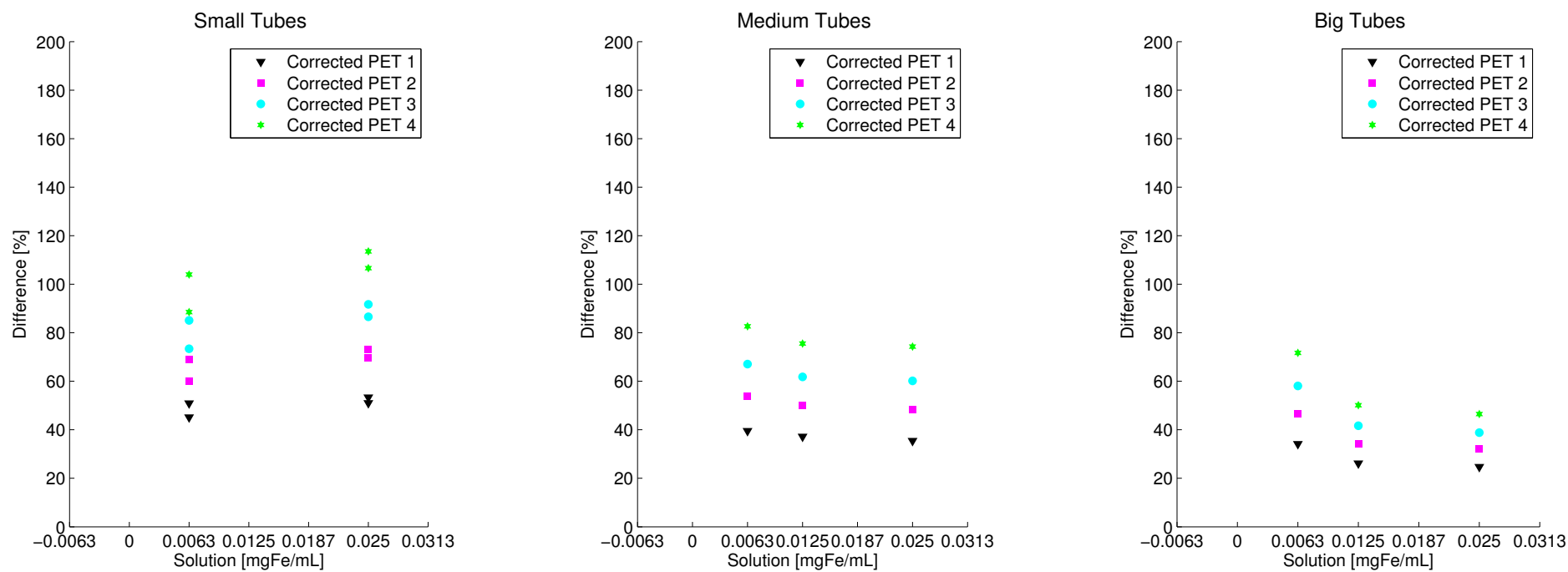


Figure 4.14: *Differences* estimated for different nanoparticles solutions and smoothing values.

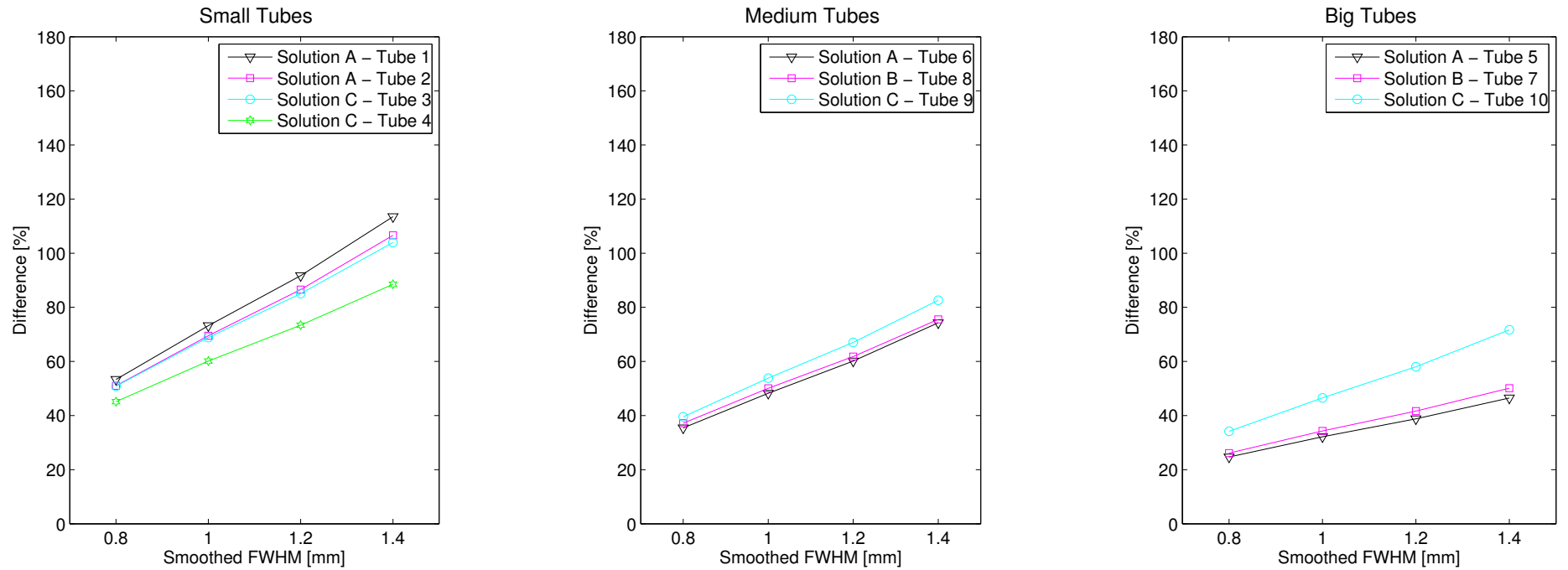


Figure 4.15: The relationship between image smoothing (FWHM in mm) and % difference of the tracer's uptake in the different tubes and solutions.

Chapter 5

Conclusion

One of the goals of this project consisted in performing a simple simulation study in order to understand how the SFSRR procedure works. In general, the use of SFSRR procedure translated into uptake improvements of 6.8 % in maximum values and 10.3% in mean values. Simulated data was created so that all slices had the same intensity, however recovered data did not show this uniformity as expected. As a result, this aspect will be clarified in future work.

Additionally, the second part of the work focused on developing an image processing protocol suitable to phantom data and then perform PVC by using the SFSRR procedure.

For this purpose, firstly SPM was evaluated for data processing. As PET and MRI data had distinct dimensions and voxel size, both datasets could not be loaded at the same time in SPM and so any translations done would lead to errors. Therefore, another processing strategy was assessed.

The second software used was AMIDE which allows to reorient and resample data, as well as to perform manual transformations. However, data reslice cannot be done according to the user requirements and as in this case PET data should have the same features than MRI, AMIDE was not selected for data processing.

In terms of the final *Image Processing Protocol* defined the following softwares were used: (i) VivoQuant; (ii) Fiji and (iii) MATLAB.

VivoQuant automatically performs data resampling and reslice. Also, it allows to reorient data and perform translations with PET and MRI datasets overlaid at the same time, minimizing any errors related with user intervention.

On the other hand, Fiji was used to create the ROI maps as it has a wide variety of shapes and tools for drawing ROIs. Another advantage is the MIJ plugin that allows a bidirectional communication between Fiji and MATLAB, guaranteeing an easy and accurate way to read and exchange data between these two softwares.

Finally, MATLAB was used to perform: (i) PET masking; (ii) estimate the mean values in the different tubes; (iii) filtering and to (iv) export data in Analyze format and double datatype.

The third and last part of this project consisted in evaluating how object size, SPIOs- ^{18}F concentrations and smoothing affected PVC in phantom data when using the SFSRR procedure.

PVEs are more significant in smaller object sizes and for greater smoothed

values. Phantom data results showed greater uptake differences when using small tubes, higher concentrations of SPIOs- ^{18}F and greater smoothing values. Also, higher uptake deviations were verified in medium and big tubes for lower solutions' concentrations and greater FWHM values.

The results obtained showed that the SFSRR procedure is efficient for minimizing the influence of PVEs in PET images, however the SFSRR package was developed to be used in brain PET images and so the parameters of the recovery model are optimized for this purpose. Therefore, several parameters will have to be changed for adapting this methodology to phantom data which will be focus of future work. Additionally, further experiments will be done in order to better understand these initial results.

To extend on the work undertaken in this thesis, it would be important to perform more simulation studies that aim to recreate certain factors that affect PET images quality and check how they affect SFSRR efficiency:

- Attenuation;
- Noise;
- Smoothing effect - the SFSRR procedure requires the use of a Gaussian filter, so different values of FWHM could be considered.

After simulations studies, phantom data analysis could be done. More specifically, it would be relevant to create an unique phantom that could be applied in all future experiments to guarantee a standard approach of data acquisition and processing. This would minimize any potential errors occurring during these two steps.

The phantom could consist in an inert medium with different holes that would recreate different object sizes, as this is one of the aspects that contributes to PVES. Then, inside of each hole different concentrations of nanoparticles associated to PET radioisotopes could be used to recreate the spill-over effect, that generally is more significant for smaller objects.

Also, it would be interesting to use distinct kinds of nanoparticles and PET radioisotopes in order to understand how they would influence the efficiency of the PVC performed.

Finally, besides exploring the recovery performed by the SFSRR procedure, other PVC methodologies could be studied, for example Lucy-Richardson deconvolution algorithm, van Cittert method and GTM (Geometrix Transfer Matix) approach, which are the most common PVC routines.

Appendix A

Simulated data - Results

Dataset	Region	Slice	Max [Bq/ml]	Difference [%]
True	Object	1 to 8	1000.0	-
PET	Object	1 to 8	800.0	-
Corrected PET	Object	1	976.0	22.0
		2	844.0	5.5
		3	798.0	-0.2
		4	784.0	-2.0
		5	780.0	-2.5
		6	806.0	0.8
		7	851.0	6.4
		8	965.0	20.6

Table A.1: Maximum values in PET and Corrected PET data and corresponding difference (%).

Dataset	Region	Slice	Mean \pm S.D. [Bq/ml]	Difference [%]
True	Object	1 to 8	1000.0 \pm 0.0	-
PET	Object	1 to 8	503.3 \pm 155.7	-
Corrected PET	Object	1	652.5 \pm 148.3	29.6
		2	558.2 \pm 119.5	10.9
		3	518.2 \pm 111.9	3.0
		4	500.7 \pm 111.0	-0.5
		5	497.4 \pm 110.3	-1.2
		6	524.6 \pm 113.2	4.2
		7	564.9 \pm 120.7	12.2
		8	642.9 \pm 146.4	27.7

Table A.2: Mean values in PET and Corrected PET data and corresponding difference (%) between both datasets.

Appendix B

Phantom data - Results

Dataset	Solution A				Solution B	
	Small tube 1	Small tube 2	Medium tube 6	Big tube 5	Medium tube 8	Big tube 7
PET	12689.7	11767.5	21873.1	35847.9	8624,0	16149.7
Corrected PET 1 (FWHM=0,8mm)	24816.0	23010.4	35812.7	55300.7	13969.5	25059.1
Corrected PET 2 (FWHM=1,0mm)	29040.0	26908.4	41462.7	63099.1	16160.7	28650.4
Corrected PET 3 (FWHM=1,2mm)	32597.4	30184.6	46436.2	69847.2	18086.6	31844.1
Corrected PET 4 (FWHM=1,4mm)	36511.9	33783.8	52106.3	77438.4	20386.9	35487.6

Dataset	Solution C			
	Small tube 3	Small tube 4	Medium tube 9	Big tube 10
PET	1241.1	1037.4	2157.7	8646.6
Corrected PET 1 (FWHM=0,8mm)	2136.2	1970.0	3478.9	14099.0
Corrected PET 2 (FWHM=1,0mm)	2483.4	2252.7	4020.6	16352.2
Corrected PET 3 (FWHM=1,2mm)	2799.7	2468.8	4437.4	18385.0
Corrected PET 4 (FWHM=1,4mm)	3169.7	2686.4	4876.6	20745.7

Table B.1: Maximum values in kBq/ml of the tubes present in PET and Corrected PET data.

Dataset	Solution A				Solution B		Solution C			
	Small tube 1	Small tube 2	Medium tube 6	Big tube 5	Medium tube 8	Big tube 7	Small tube 3	Small tube 4	Medium tube 9	Big tube 10
PET	—	—	—	—	—	—	—	—	—	—
Corrected PET 1 (FWHM=0,8mm)	95.6%	95.5%	63.7%	54.3%	62.0%	55.2%	72.1%	89.9%	61.2%	63.1%
Corrected PET 2 (FWHM=1,0mm)	128.8%	128.7%	89.6%	76.0%	87.4%	77.4%	100.1%	117.1%	86.3%	89.1%
Corrected PET 3 (FWHM=1,2mm)	156.9%	156.5%	112.3%	94.8%	109.7%	97.2%	125.6%	138.0%	105.7%	112.6%
Corrected PET 4 (FWHM=1,4mm)	187.7%	187.1%	138.2%	116.0%	136.4%	119.7%	155.4%	159.0%	126.0%	139.9%

Table B.2: Differences in the maximum values between different smoothing values, nanoparticles solutions and three sized tubes. Original PET data was used as reference, and deviations were calculated from this reference: $Difference = \left[\left(\frac{recovered\ value}{original\ value} \right) - 1 \right] \times 100\%$.

Dataset	Solution A				Solution B	
	Small tube 1	Small tube 2	Medium tube 6	Big tube 5	Medium tube 8	Big tube 7
PET	5652.6±425.9	5213.0±463.0	7691.5±637.2	12982.4±772.9	3682.2±110.2	6043.8±319.0
Corrected PET 1 (FWHM=0,8mm)	8667.6±1553.9	7871.5±1816.6	10415.5±2465.9	16186.7±3831.3	5051.2±982.8	7622.9±1968.9
Corrected PET 2 (FWHM=1,0mm)	9792.3±1965.8	8836.9±2269.7	11401.3±3087.0	17156.3±4988.8	5526.1±1278.7	8117.0±2561.6
Corrected PET 3 (FWHM=1,2mm)	10834.9±2320.1	9724.7±2657.4	12317.8±3602.0	18020.7±5995.7	5958.2±1527.4	8560.5±3081.2
Corrected PET 4 (FWHM=1,4mm)	12069.6±2731.0	10770.2±3102.0	13405.3±4178.7	19015.7±7167.4	6463.0±1808.8	9073.6±3684.9

Dataset	Solution C			
	Small tube 3	Small tube 4	Medium tube 9	Big tube 10
PET	788.5±54.4	500.3±302.4	832.4±253.6	3510.3±275.3
Corrected PET 1 (FWHM=0,8mm)	1189.8±218.9	726.1±494.5	1161.5±511.8	4709.4±1130.1
Corrected PET 2 (FWHM=1,0mm)	1331.2±271.8	801.2±570.0	1280.6±601.5	5144.3±1446.1
Corrected PET 3 (FWHM=1,2mm)	1459.3±313.6	867.4±640.3	1390.5±678.5	5548.1±1722.1
Corrected PET 4 (FWHM=1,4mm)	1608.3±358.7	943.0±724.0	1520.1±764.9	6026.8±2042.0

Table B.3: Mean values in kBq/ml of the tubes present in PET and Corrected PET data.

Dataset	Solution A				Solution B		Solution C			
	Small tube 1	Small tube 2	Medium tube 6	Big tube 5	Medium tube 8	Big tube 7	Small tube 3	Small tube 4	Medium tube 9	Big tube 10
PET	—	—	—	—	—	—	—	—	—	—
Corrected PET 1 (FWHM=0,8mm)	53.3%	51.0%	35.4%	24.7%	37.2%	26.1%	50.9%	45.2%	39.5%	34.2%
Corrected PET 2 (FWHM=1,0mm)	73.2%	69.5%	48.2%	32.2%	50.1%	34.3%	68.8%	60.2%	53.8%	46.6%
Corrected PET 3 (FWHM=1,2mm)	91.7%	86.5%	60.1%	38.8%	61.8%	41.6%	85.1%	73.4%	67.0%	58.1%
Corrected PET 4 (FWHM=1,4mm)	113.5%	106.6%	74.3%	46.5%	75.5%	50.1%	104.0%	88.5%	82.6%	71.7%

Table B.4: Differences in the mean values between different smoothing values, nanoparticles solutions and three sized tubes. Original PET data was used as reference, and deviations were calculated from this reference: $Difference = \left[\left(\frac{recovered\ value}{original\ value} \right) - 1 \right] \times 100\%$.

Bibliography

- [1] Bruce Alberts, Alexander Johnson, Julian Lewis, Martin Raff, Keith Roberts, and Peter Walter. *Molecular Biology of the Cell*. Garland Science, 4th edition, 2002.
- [2] Ichio Aoki, Chuzo Tanaka, Tetsuro Takegami, Toshihiko Ebisu, Masahiro Umeda, Masaki Fukunaga, Kohji Fukuda, Afonso C. Silva, Alan P. Koretsky, and Shoji Naruse. Dynamic activity-induced manganese-dependent contrast magnetic resonance imaging (DAIM MRI). *Magn Reson Med.*, 48(6):927–33, December 2002.
- [3] John Ashburner, Gareth Barnes, Chun-Chuan Chen, Jean Daunizeau, Guillaume Flandin, Karl Friston, Stefan Kiebel, James Kilner, Vladimir Litvak, Rosalyn Moran, Will Penny, Maria Rosa, Klaas Stephan, Darren Gitelman, Rik Henson, Chloe Hutton, Volkmar Glauche, Jérémie Mattout, and Christophe Phillips. Spm8 manual, February 2013. URL <http://www.fil.ion.ucl.ac.uk/spm/doc/manual.pdf>.
- [4] Dale L. Bailey, David W. Townsend, Peter E. Walk, and Michael N. Maisey. *Positron Emission Tomography: Basic Sciences*. Springer, 2005.
- [5] Thomas Beyer, Lutz S. Freudenberg, Johannes Czernin, and David W. Townsend. The future of hybrid imaging—part 3: PET/MR, small-animal imaging and beyond. *Insights Imaging*, 3(2):235–246, June 2011.
- [6] Richard Bitar, General Leung, Richard Perng, Sameh Tadros, Alan R. Moody, Josee Sarrazin, Caitlin McGregor, Monique Christakis, Sean Symons, Andrew Nelson, and Timothy P. Roberts. Mr pulse sequences: what every radiologist wants to know but is afraid to ask. *Radiographics*, 26(2):513–37, March-April 2006.
- [7] Anthony Blakeborough, Janice Ward, Daniel Wilson, Michelle Griffiths, Yoshiki Kajiya, J. Ashley Guthrie, and Philip J. A. Robinson. Hepatic lesion detection at MR imaging: a comparative study with four sequences. *Radiology*, 203(3):759–65, June 1997.
- [8] Norman E. Bolus, Remo George, Johnnee’ Washington, and Bradley R. Newcomer. PET/MRI: The Blended-Modality Choice of the Future? *J Nucl Med Technol.*, 37(2):63–71, June 2009.
- [9] N Boussion, M Hatt, F Lamare, Y Bizais, A Turzo, C Cheze-Le Rest, and D Visvikis. A multiresolution image based approach for correction of partial

- volume effects in emission tomography. *Physics in Medicine and Biology*, 51(7):1857–1876, March 2006.
- [10] J.E. Bowsher, Yuan Hong, L.W. Hedlund, T.G. Turkington, G. Akabani, A. Badea, W.C. Kurylo, C.T. Wheeler, G.P. Cofer, M.W. Dewhirst, and G.A. Johnson. Utilizing MRI information to estimate F18-FDG distributions in rat flank tumors. *IEEE Nuclear Science Symposium Conference Record*, 4:2488–2492, October 2004.
 - [11] Jeff W. M. Bulte and Dara L. Kraitchman. Iron oxide MR contrast agents for molecular and cellular imaging. *NMR Biomed.*, 17(7):484–99, November 2004.
 - [12] Simon R. Cherry, Angelique Y. Louie, and Russell E. Jacobs. The Integration of Positron Emission Tomography With Magnetic Resonance Imaging. *Proceedings of the IEEE*, 96(3):416–438, March 2008.
 - [13] C. Comtat, F.C. Sureau, M. Sibomana, I.K. Hong, N. Sjöholm, and R. Trebessen. Image based resolution modeling for the HRRT OSEM reconstructions software. *IEEE Nuclear Science Symposium Conference Record*, pages 4120–4123, October 2008.
 - [14] Mrinmoy De, Stanley S. Chou, Hrushikesh M. Joshi, and Vinayak P. Dravid. Hybrid magnetic nanostructures (MNS) for magnetic resonance imaging applications. *Advanced Drug Delivery Reviews*, 63(14-15):1282—1299, November 2011.
 - [15] Rafael Torres Martin de Rosales, Richard Tavaré, Rowena L. Paul, Maite Jauregui-Osoro, Andrea Protti, Arnaud Glaria, Gopal Varma, Istvan Szanda, and Philip J. Blower. Synthesis of (64)Cu(II)–Bis(dithiocarbamatebisphosphonate) and Its Conjugation with Superparamagnetic Iron Oxide Nanoparticles: In Vivo Evaluation as Dual-Modality PET–MRI Agent. *Angew Chem Int Ed*, 50(24):5509—5513, June 2011.
 - [16] Menno P. J. de Winther, Ko Willems van Dijk, Louis M. Havekes, and Marten H. Hofker. Macrophage Scavenger Receptor Class A: A Multifunctional Receptor in Atherosclerosis. *Arteriosclerosis, Thrombosis, and Vascular Biology*, 20(2):290–297, February 2000.
 - [17] Tetyana Denysenko, Luisa Gennero, Maria Augusta Roos, Antonio Melcarne, Carola Juenemann, Giuliano Faccani, Isabella Morra, Giovanni Cavallo, Stefano Reguzzi, Gianpiero Pescarmona, and Antonio Ponzetto. Glioblastoma cancer stem cells: heterogeneity, microenvironment and related therapeutic strategies. *Cell Biochemistry and Function*, 28(5):343—351, July 2010.
 - [18] Jay S. Desgrosellier and David A. Cheresh. Integrins in cancer: biological implications and therapeutic opportunities. *Nature Reviews Cancer*, 10(1):9–22, January 2010.
 - [19] M. Helena Mendonça Dias and Paul C. Lauterbur. Ferromagnetic particles as contrast agents for magnetic resonance imaging of liver and spleen. *Radiology*, 3(2):328–30, April 1986.

- [20] Jonathan A. Disselhorst, Maarten Brom, Peter Laverman, Cornelius H. Slump, Otto C. Boerman, Wim J.G. Oyen, Martin Gotthardt, and Eric P. Visser. Image-quality assessment for several positron emitters using the NEMA NU 4-2008 standards in the Siemens Inveon small-animal PET scanner. *The Journal of Nuclear Medicine*, 51(4):610–617, April 2010.
- [21] Kjell Erlandsson, Irene Buvat, P Hendrik Pretorius, Benjamin A Thomas, and Brian F Hutton. A review of partial volume correction techniques for emission tomography and their applications in neurology, cardiology and oncology. *Physics in Medicine and Biology*, 57(21):R119—R159, April 2012.
- [22] Wellcome Trust Centre for Neuroimaging UCL. SPM 8. <http://www.fil.ion.ucl.ac.uk/spm/>, February 2013. SPM8.
- [23] Charles Glaus, Raffaella Rossin, Michael J. Welch, and Gang Bao. In vivo evaluation of (64)Cu-labeled Magnetic Nanoparticles as a Dual-Modality PET/MR Imaging Agent. *Bioconjugate Chem.*, 21(4):715—722, April 2010.
- [24] Alexander Hammers, Richard Allom, Matthias J. Koepp, Samantha L. Free, Ralph Myers, Louis Lemieux, Tejal N. Mitchell, David J. Brooks, and John S. Duncan. Three-dimensional maximum probability atlas of the human brain, with particular reference to the temporal lobe. *Physics in Medicine and Biology*, 19(4):224—247, August 2003.
- [25] Mukesh G. Harisinghani, Jelle Barentsz, Peter F. Hahn, Willem M. Derseno, Shahin Tabatabaei, Christine Hulsbergen van de Kaa, Jean de la Rosette, and Ralph Weissleder. Noninvasive Detection of Clinically Occult Lymph-Node Metastases in Prostate Cancer. *N Engl J Med.*, 348(25):2491–9, June 2003.
- [26] Hans Herzog. PET/MRI: Challenges, solutions and perspectives. *Z. Med. Phys*, 22(4):281–98, December 2012.
- [27] Do Won Hwang, Hyewon Youn, and Dong Soo Lee. Molecular Imaging Using PET/MRI Particle. *The Open Nuclear Medicine Journal*, 2:186–191, 2008.
- [28] inviCRO. VivoQuant. <http://www.vivoquant.com/>, 2013. Version 1.22patch2.
- [29] Benjamin R. Jarrett, Carlos Correa, Kwan Liu Ma, and Angelique Y. Louie. In Vivo Mapping of Vascular Inflammation Using Multimodal Imaging. *PLoS One*, 5(10):e13254, October 2010.
- [30] Lucy E. Jennings and Nicholas J. Long. Two is better than one—probes for dual-modality molecular imaging. *Chem. Commun.*, (24):3511–24, June 2009.
- [31] Magdy M. Khalil. *Basic Sciences of Nuclear Medicine*. Springer, 2011.

- [32] Euitae Kim, Miho Shidahara, Charalampos Tsoumpas, Colm J McGinnity, Jun Soo Kwon, Oliver D Howes, and Federico E Turkheimer. Partial volume correction using structural-functional synergistic resolution recovery: comparison with geometric transfer matrix method. *Journal of Cerebral Blood Flow & Metabolism*, 33:914–920, March 2013.
- [33] Ha-Young Lee, Zibo Li, Kai Chen, Andrew R. Hsu, Chenjie Xu, and Xiaoyuan Chen. PET/MRI dual-modality tumor imaging using arginine-glycine-aspartic (RGD)-conjugated radiolabeled iron oxide nanoparticles. *J Nucl Med*, 49(8):1371–1379, August 2008.
- [34] Soo Hong Lee, Byung Hyo Kim, Hyon Bin Na, and Taeghwan Hyeon. Paramagnetic inorganic nanoparticles as T1 MRI contrast agents. *WIREs Nanomed Nanobiotechnol*, October 2013.
- [35] Yi-Jen Li and Alan P. Koretsky. Manganese ion enhances T1-weighted MRI during brain activation: an approach to direct imaging of brain function. *Magn Reson Med.*, 38(3):378–88, September 1997.
- [36] Zibo Li and Peter S. Conti. Radiopharmaceutical chemistry for positron emission tomography. *Advanced Drug Delivery Reviews*, 62:1031–1051, August 2010.
- [37] Chenghong Lin, Shuhui Cai, and Jianghua Feng. Positive Contrast Imaging of SPIO Nanoparticles. *Journal of Nanomaterials*, 2012:9 pages, 2012.
- [38] Erica Locatelli, Larraitz Gil, Liron Limor Israel, Lorena Passoni, Maria Naddaka, Andrea Pucci, Torsten Reese, Vanessa Gomez-Vallejo, Paolo Milani, Michela Matteoli, Jordi Llop, Jean Paul Lellouche, and Mauro Comes Franchini1. Biocompatible nanocomposite for PET/MRI hybrid imaging. *International Journal of Nanomedicine*, 7:6021—6033, December 2012.
- [39] Andreas Markus Loening and Sanjiv Sam Gambhir. AMIDE. <http://amide.sourceforge.net>, November 2012. Version 1.0.4.
- [40] Giovanni Lucignani. Nanoparticles for concurrent multimodality imaging and therapy: The dawn of new theragnostic synergies. *European Journal of Nuclear Medicine and Molecular Imaging*, 36(5):869–874, May 2009.
- [41] Jianqiao Luo, John D. Wilson, Jianyuan Zhang, Jerry I. Hirsch, Harry C. Dorn, Panos P. Fatouros, and Michael D. Shultz. A dual pet/mr imaging nanoprobe: 124i labeled $gd_{3n}@c_{80}$. *Appl. Sci.*, 2(2):465–478, May 2012.
- [42] Aldons J. Lusis. Atherosclerosis. *Nature*, 407(6801):233—241, September 2000.
- [43] Milán Magdics, László Szirmay-Kalos, Ákos Szlavec, Gábor Hesz, Balázs Benyó, Áron Cserkaszky, Judit Lantos, Szabolcs Czifrus, Dávid Légrády, András Wirth, Béla Kári3, Tamás Bükki, Gergely Patay, Dávid Völgyes, Péter Major, Gabor Nemeth4, and Balázs Domonkos. TeraTomo project: a fully 3D GPU based reconstruction code for exploiting the imaging capability of the NanoPET/CT system. In *World Molecular Imaging Congress*, April 2010.

- [44] Amir Pasha Mahmoudzadeh and Nasser H. Kashou. Evaluation of Interpolation Effects on Upsampling and Accuracy of Cost Functions-Based Optimized Automatic Image Registration. *International Journal of Biomedical Imaging*, 2013:19 pages, May 2013.
- [45] Maulik D. Majmudar, Jeongsoo Yoo, Edmund J. Keliher, Jessica J. Trulove, Yoshiko Iwamoto, Brena Sena, Partha Dutta, Anna Borodovsky, Kevin Fitzgerald, Marcelo F. Di Carli, Peter Libby, Daniel G. Anderson, Filip K. Swirski, Ralph Weissleder, and Matthias Nahrendorf. Polymeric nanoparticle PET/MR imaging allows macrophage detection in atherosclerotic plaques. *Circulation Research*, 112(5):755–761, March 2013.
- [46] Julia G Mannheim, Martin S Judenhofer, Andreas Schmid, Julia Tillmanns, Detlef Stiller, Vesna Sossi, and Bernd J Pichler. Quantification accuracy and partial volume effect in dependence of the attenuation correction of a state-of-the-art small animal PET scanner. *Physics in Medicine and Biology*, 57(12):3981—3993, May 2012.
- [47] Cynthia A. Massaad and Robia G. Pautler. Manganese-enhanced magnetic resonance imaging (MEMRI). *Methods Mol Biol.*, 11:145—174, 2011.
- [48] MathWorks. MATLAB. <http://www.mathworks.co.uk/products/matlab/>, August 2013. Version R2013b.
- [49] Donald W. McRobbie, Elizabeth A. Moore, Martin J. Graves, and Martin R. Prince. *MRI: from Picture to Proton*. Cambridge University Press, second edition, 2006.
- [50] Karen S. Meir and Eran Leitersdorf. Atherosclerosis in the Apolipoprotein E-Deficient Mouse: A Decade of Progress. *Arteriosclerosis, Thrombosis, and Vascular Biology*, 24(6):1006–1014, April 2004.
- [51] Sung min Kim, Min Kyung Chae, Min Su Yim, Il Ha Jeong, Janggeun Cho, Chulhyun Lee, and Eun Kyoung Ryu. Hybrid PET/MR imaging of tumors using an oleanolic acid-conjugated nanoparticle. *Biomaterials*, 34(33):8114–8121, November 2013.
- [52] Enrique Morales-Avila, Guillermina Ferro-Flores, Blanca E. Ocampo-García, and Flor de María Ramírez. *Molecular Imaging*, chapter Radio-labeled Nanoparticles for Molecular Imaging, pages 15–38. InTech, 2012.
- [53] Hyon Bin Na, In Chan Song, and Taeghwan Hyeon. Inorganic Nanoparticles for MRI Contrast Agents. *Adv. Mater.*, 21:2133—2148, June 2009.
- [54] Ying-Hwey Nai. Partial volume correction pvc_sfsrr. Manual, March 2013. URL http://www.noninvasive.med.tohoku.ac.jp/ShidaharaLab/PVC_SFSRR_Manual.pdf.
- [55] Luca Persano, Elena Rampazzo, Giuseppe Basso, and Giampietro Viola. Glioblastoma cancer stem cells: role of the microenvironment and therapeutic targeting. *Biochemical Pharmacology*, 85(5):612—622, March 2013.

- [56] Bernd J. Pichler, Hans F. Wehrl, Armin Kolb, and Martin S. Judenhofer. Positron Emission Tomography/Magnetic Resonance Imaging: The Next Generation of Multimodality Imaging? *Seminars in Nuclear Medicine*, 38(3):199–208, May 2008.
- [57] Robert A. Pooley. AAPM/RSNA physics tutorial for residents: fundamental physics of MR imaging. *Radiographics*, 25(4):1087–99, July-August 2005.
- [58] Peter Reimer, Paul M. Parizel, James F.M. Meaney, and Falko A. Stinchnoth. *Clinical MR Imaging: A Practical Approach*. Springer, second edition, 2006.
- [59] Oliver G. Rousset, Yilong Ma, and Alan C. Evans. Correction for partial volume effects in PET: principle and validation. *The Journal of Nuclear Medicine*, 39(5):904–911, May 1998.
- [60] Olivier Rousset, Arman Rahmim, Abass Alavi, and Habib Zaidi. Partial Volume Correction Strategies in PET. *PET Clinics*, 2(2):235–249, April 2007.
- [61] Daniel Sage, Dimiter Prodanov, Jean-Yves Tinevez, and Johannes Schindelin. MIJ. <http://bigwww.epfl.ch/sage/soft/mij/>. Version 8.2.0.701.
- [62] S. Sastry and R. E. Carson. Multimodality bayesian algorithm for image reconstruction in positron emission tomography: a tissue composition model. *IEEE Transactions on Medical Imaging*, 16(6):750–761, December 1997.
- [63] Johannes Schindelin, Ignacio Arganda-Carreras, Erwin Frise, Verena Kaynig, Mark Longair, Tobias Pietzsch, Stephan Preibisch, Curtis Rueden, Stephan Saalfeld, Benjamin Schmid, Jean-Yves Tinevez, Daniel James White, Volker Hartenstein, Kevin Eliceiri, Pavel Tomancak, and Albert Cardona. Fiji. <http://fiji.sc/Fiji>. Version 1.3.6.
- [64] Volkmar Schulz, Bjoern Weissler, Pierre Gebhardt, Torsten Solf, Christoph W. Lerche, Peter Fischer, Michael Ritzert, Viacheslav Mlotok, Claudio Piemonte, Benjamin Goldschmidt, Stefaan Vandenberghe and Andre Salomon, Tobias Schaeffter, and Paul M. Marsden. SiPM based preclinical PET/MR insert for a human 3T MR first imaging experiments. *IEEE Nuclear Science Symposium and Medical Imaging Conference (NSS/MIC)*, pages 4467–4469, October 2011.
- [65] Udo Schwertmann and Rochelle M. Cornell. *Iron Oxides in the Laboratory, Preparation and Characterization*. WILEY-VCH, second edition, 2000.
- [66] Ramesh Sharma, Youwen Xu, Sung Won Kim, Michael J. Schueller, David Alexoff, S. David Smith, Wei Wang, and David Schlyer. Carbon-11 radiolabeling of iron-oxide nanoparticles for dual-modality PET/MR imaging. *Nanoscale*, 5(16):7476–7483, August 2013.
- [67] M Shidahara, C Tsoumpas, C J McGinnity, T Kato, H Tamura, A Hammers, H Watabe, and F E Turkheimer. Wavelet-based resolution recovery using an anatomical prior provides quantitative recovery for human population phantom PET (11C)raclopride data. *Physics in Medicine and Biology*, 57(10):3107–3122, May 2012.

- [68] Miho Shidahara, Charalampos Tsoumpas, Alexander Hammers, Nicolas Boussion, Dimitris Visvikis, Tetsuya Suhara, Iwao Kanno, and Federico E. Turkheimer. Functional and structural synergy for resolution recovery and partial volume correction in brain PET. *NeuroImage*, 44(2):340—348, January 2009.
- [69] Jin sil Choi, Jeong Chan Park, Hyunsoo Nah, Seungtae Woo, Jieun Oh, Kyeong Min Kim, Gi Jeong Cheon, Yongmin Chang, Jeongsoo Yoo, and Jinwoo Cheon. A hybrid nanoparticle probe for dual-modality positron emission tomography and magnetic resonance imaging. *Angewandte Chemie International Edition*, 47(33):6259—6262, August 2008.
- [70] Afonso C. Silva, Jung Hee Lee, Ichio Aoki, and Alan P. Koretsky. Manganese-enhanced magnetic resonance imaging (MEMRI): methodological and practical considerations. *NMR Biomed.*, 17(8):532—543, December 2004.
- [71] G. J. Slater, S. Saini, W. W. Mayo-Smith, P. Sharma, and P. J. Eisenberg and P. F. Hahn. Mn-DPDP enhanced MR imaging of the liver: analysis of pulse sequence performance. *Clinical Radiology*, 51(7):484–6, July 1996.
- [72] Marine Soret, Stephen L. Bacharach, and Irene Buvat. Partial-volume effect in PET tumor imaging. *The Journal of Nuclear Medicine*, 48(6):932–945, June 2007.
- [73] Paul Suetens. *Fundamentals of Medical Imaging*. Cambridge University Press, second edition, 2009.
- [74] Bendzsel Tamás. nanoScan PET/MRI. Brochure, April 2012. URL <http://www.mediso.com/uploaded/NMB.10.12-web.pdf>.
- [75] Boon-Keng Teo, Youngho Seo, Stephen L. Bacharach, Jorge A. Carrasquillo, Steven K. Libutti, Himanshu Shukla, Bruce H. Hasegawa, Randall A. Hawkins, and Benjamin L. Franc. Partial-volume correction in PET: validation of an iterative postreconstruction method with phantom and patient data. *The Journal of Nuclear Medicine*, 48(5):802–810, May 2007.
- [76] Kris Thielemans, Charalampos Tsoumpas, Sanida Mustafovic, Tobias Beisel, Pablo Aguiar, Nikolaos Dikaos, and Matthew W Jacobson. STIR. <http://stir.sourceforge.net/>. Version 2.4.
- [77] Benjamin Aneurin Thomas. *Improved brain PET quantification using partial volume correction techniques*. PhD thesis, UCL, London,UK, March 2012.
- [78] Daniel L J. Thorek, Anthony K. Chen, Julie Czupryna, and Andrew Tsourkas. Superparamagnetic iron oxide nanoparticle probes for molecular imaging. *Ann Biomed Eng.*, 34(1):23–38, January 2006.
- [79] Jussi Tohka and Anthonin Reilhac. Deconvolution-based partial volume correction in Raclopride-PET and Monte Carlo comparison to MR-based method. *The Journal of Nuclear Medicine*, 39(4):1570—1584, February 2008.

- [80] Chuqiao Tu, Thomas S. C. Ng, Russell E. Jacobs, and Angelique Y. Louie. Multimodality PET/MRI agents targeted to activated macrophages. *J Biol Inorg Chem*, October 2013.
- [81] James E. Turner. *Atoms, Radiation and Radiation Protection*. WILEY-VCH, third edition, 2007.
- [82] Iris Verel, Gerard W. M. Visser, and Guus A. van Dongen. The Promise of Immuno-PET in Radioimmunotherapy. *The Journal of Nuclear Medicine*, 46(1 (Suppl)):164–171, January 2005.
- [83] Christian Weber and Heidi Noels. Atherosclerosis: current pathogenesis and therapeutic options. *Nature Medicine*, 17(11):1410—1422, November 2011.
- [84] Ralph Weissleder, David D. Stark, Barry L. Engelstad, Bruce R. Bacon, Carolyn C. Compton, David L. White, Paula Jacobs, and Jerome Lewis. Superparamagnetic iron oxide: pharmacokinetics and toxicity. *American Journal of Roentgenology*, 152(1):167–73, January 1989.
- [85] Michael J. Welch, Craig J. Hawker, and Karen L. Wooley. The Advantages of Nanoparticles for PET. *J Nucl Med*, 50(11):1743–1746, November 2009.
- [86] Xiaoqiang Yang, Hao Hong, Jamison J. Grailer, Ian J. Rowland, Alireza Javadi, Samuel A. Hurley, Yuling Xiao, Yunan Yang, Yin Zhang, Robert J. Nickles, Weibo Cai, Douglas A. Steeber, and Shaoqin Gong. cRGD-functionalized, DOX-conjugated, and (64)Cu-labeled superparamagnetic iron oxide nanoparticles for targeted anticancer drug delivery and PET/MR imaging. *Biomaterials*, 32(17):4151—4160, June 2011.
- [87] Hyeona Yim, Seogjin Seo, and Kun Na. MRI Contrast Agent-Based Multifunctional Materials: Diagnosis and Therapy. *Journal of Nanomaterials*, 2011:11 pages, 2011.
- [88] Habib Zaidi and ALberto Del Guerra. An outlook on future design of hybrid PET/MRI systems. *Med. Phys.*, 38(10):5667–891, October 2011.